**FACULTY OF SCIENCE AND TECHNOLOGY**

# MASTER THESIS

| | |
|---|---|
| Study programme / specialisation:<br>**Petroleum engineering/ Petroleum, process and production engineering** | The spring semester, 2022<br><br>Open |
| Author:<br>**Nazila Engarnevis** | Signature:<br>Nazila Engarnevis |
| Course coordinator:<br><br>Supervisor(s):<br>**Steinar Evje, Johan Olav Helland** | |
| Thesis title:<br>**"A pore-to-core scale investigation of hysteresis for CO2 storage processes using a discrete-domain method"** | |
| Credits (ECTS): **30** | |
| Keywords:<br>CO2 sequestration<br>Capillary trapping<br>Hysteresis<br>Displacement<br>Discrete-domain method<br>Pressure-controlled<br>Saturation-controlled | Pages: 67<br><br>Stavanger, 2022 |

Table of Contents

# Acknowledgements

"Every story has an end, but in life, every ending is just a new beginning…"

Uptown girls

With this thesis, I would like to conclude my two years of studies as a master's student in petroleum, process and production engineering at the University of Stavanger, however, the choice of this thesis has set in motion an eager interest for me to dig deeper into the physics of multiphase fluid flow in porous media. I hope that in the near future, my work would contribute to the matter of CCUS.

For this great opportunity, I would like to thank my supervisors, Prof. Steinar Evje and Dr. Johan Olav Helland who trusted me with their project and prepared the grounds for me to commence my studies. Their broad knowledge, kind attitude and genuine support and encouragement paved my way and made this study a much more pleasing experience.

I would like to express my everlasting gratitude to my mom, dad and my brother, to whom I owe all that I have. They never gave up on me and without their sacrifices, in every possible way, I would not have been the person that I am today.

Last but not least, I would like to thank, Mr. Fahmin Husuzade. Classmate turned best friend, he selflessly was there for me through thick and thin when I needed support in a new, stranger world after I moved to Norway. I wish him the best in life!

# List of Figures

# List of Tables

# Abstract

In this thesis we have studied a discrete-domain method that is implemented to demonstrate the immiscible, two-phase displacements of two fluids, namely CO2 and water (or brine) in an originally water-saturated reservoir (an aquifer). The method provides a model that is based on a free energy density function that gives a thermodynamic explanation of the dynamics of the interface between the fluids and describes the rugged energy landscape that represents the reversible and irreversible transition states of the interface through metastable states and energy barriers. Furthermore, in this model a discretization of the reservoir into a number of compartments has been done and the model simulates the flow system in terms of the capillary pressure and the local water compartment saturations. This model works based on the theory that these compartments are weakly connected via an external drive, e.g., a fixed imposed capillary pressure or injection rate of CO2. The main purpose of this study is to investigate hysteresis in the drainage and imbibition processes both in the capillary pressure and local water saturation curves with regards to the global water saturation.

# Chapter 1. Introduction

It is an indisputable fact that with the current immoderate and ever-increasing concentrations of the anthropogenic $CO_2$ in the atmosphere, only a remarkable plummet in the emissions can halt the sharply elevating ratios of this greenhouse gas affecting the Earth's climate (R. Juanes et al., 2006). Among the existing $CO_2$ sequestration methods, the injection of $CO_2$ into the geological formations seems to be a highly effective and promising solution (Ershadniaa et al., 2021). Various geological formations can be considered as the injection target of $CO_2$, such as the depleted hydrocarbon reservoirs, deep saline aquifers and unmineable coal seams (Sedaghatinasab et al., 2021).

Despite the EOR advantages of $CO_2$ injection into the oil and gas reservoirs, deep saline or brine-saturated aquifers are known to be the best targets in terms of $CO_2$ storage capacity (Akbarabadi & Piri, 2013). Reports show that these aquifers contain an average amount of 400-10,000 Gt worth of capacity for $CO_2$ storage. (Gale, 2004) Therefore, the latter is the subject of this study.

The path that the $CO_2$ traverses from the moment of injection to its final state is of great importance when simulating the migration and entrapment of $CO_2$ (Zweigel et al., 2000). The buoyant, density-driven upward convection flow of $CO_2$ will most probably be hindered by the sealing formation layer or/ and other trapping mechanisms at some point (Pham et al., 2013).

The greatest concern about the geological $CO_2$ storage is the leak potential of the injected $CO_2$. Therefore, it is important to know the flow and distribution patterns of the gas and its characterization (Mortezaei et al., 2018). Note that the injected $CO_2$ is in super-critical conditions during injection and at the depths of the target formation,

however, for simplicity, it is referred to as gas in this thesis (R. Juanes et al., 2006). There are four mechanisms for the sequestration of CO2 (Hassanzadeh et al., 2009) as listed in table 1.1:

(I) *Structural and stratigraphic/ hydrodynamic trapping*, where the injected CO2 migrates upwards due to buoyancy while probably keeping its continuous form of a plume until it reaches the relatively non-permeable caprock where it is trapped (Hesse & Woods, 2010).

(II) *Residual (capillary) trapping*, where the migrating CO2 plume starts to disconnect on its extremity as a result of a displacement process named "imbibition", creating trails of disconnected, stagnant CO2 blobs behind in a water-wet reservoir. On a pore-scale, the equivalent would be the disconnected, immobile and randomly distributed pore-sized flecks of CO2 trapped in the middle of the larger water-wet pores (Krevor et al., 2015). This mechanism will be further elaborated in the following paragraphs. There are generally two competing displacement mechanisms that contribute to capillary trapping: Pore-filling displacement and snap-off which will be explained in the following pages (Singh et al., 2017).

(III) *Solubility trapping*, where the injected CO2 is dissolved in the brine resulting in an acidic solution. Several parameters affect this method such as the formation temperature and pressure, salinity of the brine, etc. Nevertheless, the dissolution rate is usually enhanced due to the higher density of the brine-CO2 mixture (Akbarabadi & Piri, 2013).

(IV) *Mineral trapping*, where the acidic solution from the previous mechanism reacts geomechanically with specific minerals in the formation producing

new minerals that will eventually precipitate. CO2 sequestration by mineralization can be considered as a relatively permanent and therefore safe trapping method (Hadi Mosleh et al., 2019).

| Trapping method | Description | Sequestration rate |
|---|---|---|
| Hydrodynamic | Impediment of the CO2 upward migration due to a non-permeable caprock | Fast |
| Residual/ Capillary | Entrapment of the CO2 in larger pores in the form of CO2 blobs and ganglia as a result of the piston-like and snap-off displacement mechanisms | Fast |
| Solubility | Dissolution of the CO2 gas in the brine bed resulting in a heavier, acidic solution | Slow |
| Mineral | Geochemical reaction of the CO2-brine acidic mixture with the minerals from the formation that it comes in contact with | Very slow |

*Table 1.1. CO2 geological sequestration methods*

In terms of the duration of each of the sequestration processes, it can be said that the first two methods, the hydrodynamic and the capillary trappings, are known to occur in shorter timescales in comparison with the two latter, with mineral trapping being the slowest, due to the very slow precipitation reaction rates. (R. Juane et al., 2006)

Characterization of both, the hydrodynamic and the capillary trapping methods is completely based on the multiphase flow dynamics in the porous media which are affected by the hysteresis in the system.

Consider a brine-saturated reservoir as mentioned earlier, where the CO2, as the non-wetting phase, is being injected, displacing the brine, i.e., the wetting phase. As the CO2 is injected, the fraction of the pore-space that is occupied by the brine (the saturation of the wetting phase, $S_w$) is reduced, giving its place to the incoming CO2, increasing the non-wetting saturation, $S_{nw}$. This process is called drainage. The

mechanism that defines the displacement of the CO2-brine interface is called "pore-filling" or "piston-like", i.e., the CO2 invades the brine-saturated pores via entering and crossing the pore-throats by pushing the brine in a piston-like manner (Helland et al., 2017). However, after the injection is completed, the injected CO2 migrates towards the top of the formation while sustaining its continuous form as much as possible.

The lack of the pressure in the void space behind causes the brine to substitute and displace CO2 in the plume's tail-ends. The process where the raise in the wetting phase and the depletion in the non-wetting phase saturations occur is called imbibition (Benson et al., 2015).

By displacing the plume's trailing edges during imbibition, the brine entraps the CO2 in the centre of the larger pore-space which is coated by water due to the reservoir's strong wetting preferences towards the brine.

On a pore scale, this mechanism is named "snap-off", that is during the imbibition of a water-wet pore that is already invaded by the CO2, the water film along the pore walls thickens, finally meeting and cutting off the nonwetting CO2 at the pore throats, allowing these throats to fill with water (Helland et al., 2017).

The trapped CO2 flecks are disconnected from their stream and remain static in the form of CO2 ganglia and blobs. The above description demonstrates how the residual trapping mechanism works (Hunt & Sitar, 1988).

Capillary trapping has a significant influence on the CO2 migration and distribution pathways, which eventually affects all sequestration methods. It is in fact, one of the main sources of the irreversibility and path-dependence in the multiphase flow behaviour, a phenomenon known as hysteresis.

This hysteretic manner is exhibited by the relative permeabilities of the non-wetting phase as well as the capillary pressures which depend on the saturation history of the porous media (Spiteri et al., 2005). (Note that capillary pressure, $P_c$, refers to the difference between the pressures of the non-wetting- and the wetting phases, respectively, $P_c = P_{nw} - P_w$.) (McPhee et al., 2015)

As mentioned, one of the major causes of the hysteretic behaviour at the pore-scale is the residual trapping of the non-wetting phase. However, there can be another cause of hysteresis in the drainage and imbibition processes that does not involve residual trapping. And that is, in drainage, when the CO2-brine interface reaches a narrow pore-throat, it is stopped until the capillary pressure is high enough for it to infiltrate. So, its motion is governed by the size and ratio of the throats. On the contrary, in imbibition, when it traverses the pore-throat, its motion, which is now governed by the pore size, is paused at the entrance of the larger pores until the capillary pressure decreases to a level low enough for it to continue (Helland et al., 2017).

So, all in all, it is the complexity in the pore medium's geometry, i.e., the variabilities in the pore's throat-to-body ratios as well as their size and shape distribution that determines the winner in the rivalry between the piston-like and the snap-off mechanisms and ends in the drainage and imbibition not being reversible and thus leads to hysteresis (Singh et al., 2017).

Another thing to consider is the contact angle hysteresis. In other words, the advancing and receding contact angles between the wetting fluid and the solid surface of the pores are different during imbibition and drainage, respectively; See figure 1.1. This happens because of the altering surface properties of the pores and pore-throats such as their roughness (Gao & McCarthy, 2006).

Note that the contact angle or the wetting angle is the angle that the wetting phase forms between the solid surface of the pore and the plane tangential to the interface of the two fluids that passes through the three-phase (fluid-fluid-solid) line of contact.

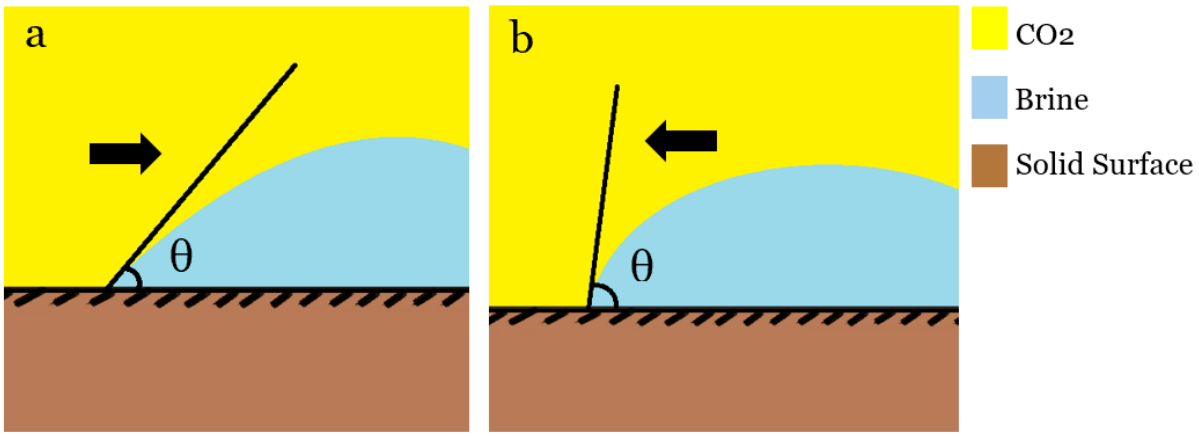


*Figure 1.1. (a) The receding contact angle of the wetting phase during drainage is smaller than (b) the advancing contact angle of the wetting phase during imbibition; This is an indicator of hysteresis in contact angles*

So, in short, in a two-phase system which is the subject of this study, during the back-and-forth drainage and imbibition stages, the non-wetting phase (the CO2 gas) is partly entrapped in the pore-space by the wetting phase (the brine) due to the rocks' wettability preferences towards the brine. This occurrence, along with the aforementioned influence of complex geometry as well as the varying contact angles lead to hysteresis in relative permeabilities of the non-wetting phase, ultimately affecting the fluids' distribution in the formation. Therefore, accounting for hysteresis is actually very important in simulations of multiphase flow in porous media. (R. Juanes et al., 2006)

# Chapter 2. Physics and Thermodynamics of Capillary

The two-phase or in general the multiphase flow in porous media refers to the *dynamic*, immiscible fluid phases that are present in the reservoir. In this thesis the two phases are, as mentioned earlier, the super-critical CO2 or simply gas and the brine which for ease of simulations are assumed to be immiscible.

For a better understanding of the fluid dynamics on a pore-scale, a porous medium simplistically can be represented as a capillary tube with non-uniform diameter along its axis which is connected to a brine-saturated reservoir on its right-hand side and a CO2-saturated medium, such as a CO2 reservoir, on its left-hand side (Cueto-Felgueroso & Juanes, 2016); See figure 2.1.

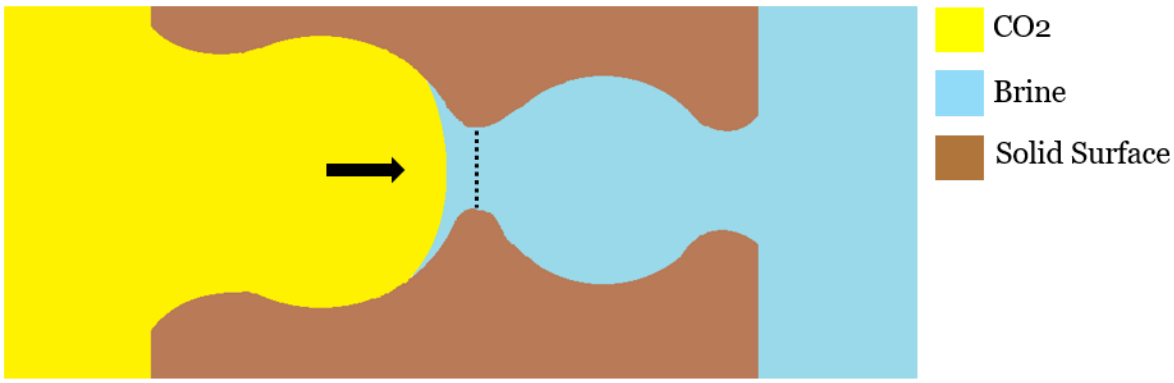


*Figure 2.1. Representation of the porous media as a non-uniform capillary tube and demonstration of the two-phase fluid displacements between the gas and the brine inside the pore space. The pores are connected to a gas-saturated reservoir on the left and a brine-saturated reservoir on the right.*

As seen in figure 2.1, during drainage, that is when the CO2 is being injected, the capillary pressure is increased as the non-wetting phase's pressure, $P_{nw}$ is raised. This causes the interface or the meniscus between the two phases to move towards right, increasing the non-wetting phase saturation, $S_{nw}$. During this shift and before

reaching a narrow-enough pore throat (Shown in figure 2.1 with the dotted line), the interface of the fluids is able to exhibit equilibrium after each incremental step in the rising capillary pressure, resulting in a smooth reversible flow.

When the meniscus reaches the dotted line, which as mentioned is representative of narrow pore-throat, the next step in pressure elevation will push it as a consequence of a rather sudden reconfiguration, to a location where the radius corresponds to the imposed external force by reaching a steady state of equilibrium again. This interfacial jump, known as a Haines jump (Sun & Santamarina, 2019) is an indicator of the irreversible nature of the system and eventually hysteresis.

Any intermediate location for the interface would be unstable as it does not correspond to an equilibrium state. The displacements, in consistence with the capillary pressure of the state, will carry on following the same mechanism throughout the porous media. The behaviour of the system has a similar explanation in the opposite direction, that is during imbibition (Cueto-Felgueroso & Juanes, 2016).

The continuous, stepwise change in the capillary pressure or the saturation of the non-wetting phase causes reversible displacements of the meniscus. These events are named as isons. On the contrary, the abrupt changes or reconfigurations of the interface following the swift pore occupations are referred to as rheons (Morrow, 1970).

It is worth mentioning that the slow and laminar flow regime that is proceeding at the pore-scale in the reservoir and away from the injection wells is considered to be capillary-dominated. This can be quantified by the capillary number, $Ca = Viscous\ force/Capillary\ force$. When $Ca < 10\text{^}(-6)$, which is the assumption in this study, it indicates that the capillary forces are dominant over the viscous forces in the porous media, eventually ensuring that multiple stable states can describe the flow,

since the flow rates are not considered so high that there would not be any stable states (AbdusSatter & Ghulam M.Iqbal, 2016).

The occurrence of multiple stable states in the pore flow in addition to the existence of unstable, intermediary states between each equilibrium locus characterize the multi-stability and metastability features in the pore-scale, immiscible multiphase flow, which again point to hysteresis (Cueto-Felgueroso & Juanes, 2016).

So far, we have demonstrated an image of the immiscible, two-phase displacements at the pore-scale. Yet, for understanding the physics of these systems, a thermodynamic explanation of the surface energetics of the interfaces between each two phases, is required. To elucidate this argument, the concepts of interfacial tension, the Young-Laplace and the Young equations have been described below (Morrow, 1970; Blunt, 2017)

## 2. 1. Interfacial tension

Interfacial tension, $\sigma$, is the energy, $F$, associated with the interface of two phases, fluid or solid, per unit area of it, or the change in the free energy (for a system with a specified pressure, this potential would be Gibbs free energy) for a given change in surface area of the interface, $\sigma = dF/dA$.

In each phase, there are inter-molecular bonds with specific levels of energies, holding together and forming that phase. When two immiscible phases encounter, an interface between them is created, and the inter-molecular bonds at the surface of contact break, releasing energy until equilibrium is reached. The equilibrium state is where the free energy density or $\sigma$ is minimum.

For instance, when a water droplet lays upon a solid surface, depending on how hydrophobic the surface's material is, the droplet's shape is sustained at equilibrium, in a form that minimizes the interfacial surface area of contact. And since there is energy associated with this interface, the interfacial energy is minimized as well.

## 2. 2. The Young-Laplace equation

The Young-Laplace equation is an equation that is used to find the pressure difference between two fluid phases at their interface. At the pore-scale displacements, this equation comes from an energy balance. When one phase exerts a constant pressure on the other, for instance water against the CO2, there exists a pressure difference between the two phases, which as mentioned before is known as the capillary pressure, $P_c = P_{nw} - P_w$. The work done or the energy put into the system, $(P_{nw} - P_w)\, dV$, creates interfacial area between the phases with an energy, $\sigma\, dA$.

$$P_c\, dV = \sigma\, dA \qquad \textit{(Eq. 1)}$$

$$P_c = \sigma\, \frac{dA}{dV} \qquad \textit{(Eq. 2)}$$

For a slight expansion of a fluid-fluid interface with curvature radii of $r_1$ and $r_2$ and a total surface curvature of $\kappa$, the Young-Laplace equation will derive to be (Blunt, 2017, pp. 4-7):

$$P_c = \sigma \left(\frac{1}{r_1} + \frac{1}{r_2}\right) = \kappa\, \sigma \qquad \textit{(Eq. 3)}$$

When the fluids are at the state of equilibrium and therefore still, each fluid exhibits a constant pressure and hence giving a fixed capillary pressure, which evidently leads to a fixed curvature, $\kappa$, despite the spatial variations that the radii may have.

## 2. 3. The Young equation

The Young equation is another energy balance like the Young-Laplace equation, with the difference that it introduces a solid surface to investigate the arrangement of the curved interfaces in the voids of a solid porous medium. So, its purpose is to find the position of the two phases at rest on a solid surface at a fixed volume. The energy change here can be viewed as a tension and therefore the energy balance would become a balance of forces at the fluid-fluid-solid interface. In figure 2.2, we see the blow up of how two fluids hit the solid surface at a distinct contact angle, $\theta$, and a diagram of the interfacial tensions between each two phases at the three-phase contact line. A simple horizontal force balance at this point derives the Young equation:

$$\sigma_{nws} = \sigma_{ws} + \sigma \cos\theta \qquad \textit{(Eq. 4)}$$

$$\cos\theta = \frac{\sigma_{nws} - \sigma_{ws}}{\sigma} \qquad \textit{(Eq. 5)}$$

Where $\sigma_{nws}$ is the interfacial tension between the solid and the non-wetting fluid, $\sigma_{ws}$ the interfacial tension between the solid and wetting fluid and $\sigma$ the fluid-fluid interfacial tension.

This leads to the definition of wettability which identifies the different interactions between a fluid and a solid surface. The contact angle is measured through the denser phase, typically water. The values that the contact angle gets, suggest how wetting a fluid is towards a solid surface. Table 2.1 demonstrates variations of wettability based on the contact angle.

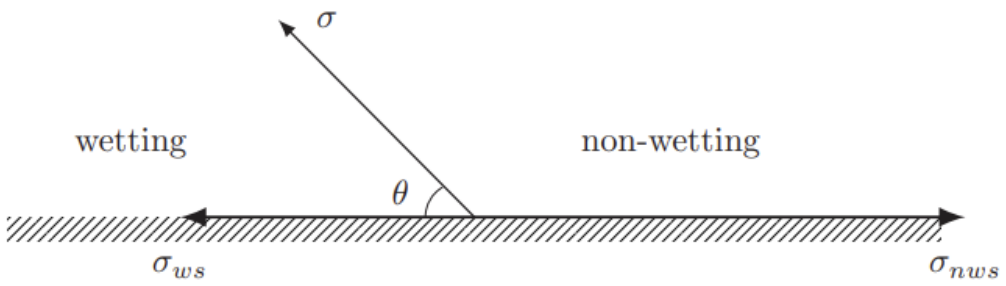


*Figure 2.2. The interfacial tension diagram for the situation of two fluid phases in contact with a solid; A horizontal force balance yields the Young equation*

| **Contact angle** | =0 | <90 | =90 | >90 | =180 |
|---|---|---|---|---|---|
| **Wettability** | Completely water-wet | Water-wet | Neutrally wet | Oil-wet | Completely oil-wet |

*Table 2.1. Variations of wettability according to the contact angle*

## 2. 4. Thermodynamic description

The contact angle that is measured when the system is at rest, does not represent the contact angle of displacement which is what we need to put in our models and to characterize the displacement. To infer this and also to define wettability and analyse the displacements we will derive another energy balance at the pore scale. Figure 2.3 is another demonstration of the displacements in the porous medium. Imagine phase 1 is the wetting phase displacing phase 2, the

non-wetting phase at a contact angle of $\theta$ that is consistent with the change in the interfacial free energy, $dF$. The mechanical work we put in, injecting fluids so that one phase displaces another as we mentioned is $PdV$. For the two phases here, and since phase 1 is displacing phase 2, this work will eventually become $P_1\ dV_1 - P_2\ dV_1 = -P_c\ dV_1$ (from the definition of capillary pressure we have: $P_c = P2 - P1$).

$dV1$ can be written as $dV_1 = \phi\ V\ \Delta S_1$, where $\phi$ is the porosity, $V$ is the total bulk volume of the rock and the pore space, and $\Delta S_1$ is the change in the wetting phase saturation. From the Young-Laplace equation we remember that $P_c = (\kappa_1 + \kappa_2)\ \sigma = \kappa\ \sigma$ , with $\kappa$ being the total curvature. The contribution of the mechanical work to the free energy of displacement will be $dF_1$.

$$dF_1 = -P_c\ dV_1 = -\kappa\ \sigma\ \phi\ V\ \Delta S_1 \qquad \textit{(Eq. 6)}$$

Another contribution to $dF$, is the changes in the free energies associated with the areas of the interfaces, $dF_2$:

$$dF_2 = \sigma\ \Delta A_{12} + (\sigma_{1s} - \sigma_{2s})\Delta A_{1s} \qquad \textit{(Eq. 7)}$$

$\Delta A_{12}$ and $\Delta A_{1S}$ are the changes in the areas of the fluid 1-fluid 2 and fluid 1-solid meniscus or the interfaces during this displacement. From the Young equation we can write:

$$dF_2 = \sigma\, \Delta A_{12} + (\sigma_{1s} - \sigma_{2s})\Delta A_{1s} = \sigma\, \Delta A_{12} - \sigma \cos\theta\, \Delta A_{1s} \qquad (Eq.\ 8)$$

The interfacial area, $A$, is usually written in the form of specific interfacial area, $a$, which is $a = A/V$. Summing up $dF_1$ and $dF_2$ will give the change in free energy, $dF$:

$$dF = -\kappa\, \sigma\, \phi\, V\, \Delta S_1 + \sigma\, \Delta a_{12}\, V - \sigma \cos\theta\, \Delta a_{1s}\, V \qquad (Eq.\ 9)$$

A general assumption in this energy balance is that no energy is lost (no viscous dissipation) in the displacements because the movement of the fluids is slow enough to be approximated as a series of equilibrium states.

Equation 9 represents the available energy of the interface of the system according to Gibbs, which is the surface's reversible work for extension. This potential can be interpreted as the increase in the Gibbs or the Helmholtz free energy of the system under prescribed circumstances which we represent here by the change in the free energy of the system per unit area of the interface, $dF/dA$ (Morrow, 1970). In the following chapter, we will discuss a method which is based on the minimization of the interfacial free energy, to characterize the dynamics of the two-phase fluid flow in the porous medium.

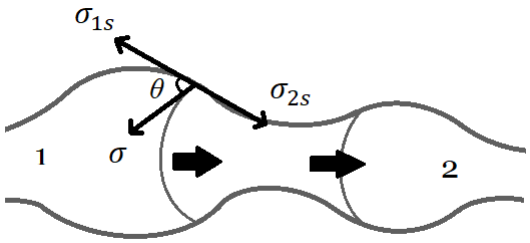


*Figure 2.3. The interfacial tension diagram for the two-phase displacements at the pore-scale*

# Chapter 3. Methodology

The model that is provided in this study to simulate the two-phase flow in a reservoir, is built upon the hypothetical representation of the porous media that was provided in figure 2.1 and is taken from the studies of (Cueto-Felgueroso & Juanes, 2016). We consider a representative elementary volume (REV) of the reservoir that we are about to study, and we discretise it into a number of compartments, $i = 1, \dots, N$, with equal bulk volumes. The purpose will then break down to the analysis of the fluids entering and exiting each of these compartments.

The first critical assumption would be that each compartment has a weak connection to the surrounding compartments due to either a shared, externally imposed capillary pressure or an injection rate constraint (here a fixed saturation). This assumption divides our simulation into two main categories of displacement modes or protocols: Pressure-controlled displacement and saturation-controlled displacement. The description of each is provided in table 3.1.

| **Displacement Protocol** | **Description** |
|---|---|
| Pressure-controlled | Displacements driven by fixed incremental changes in the imposed capillary pressures |
| Saturation-controlled | Displacements driven by applying a constraint on the non-wetting phase's saturation via imposing fixed incremental changes in the CO2 injection/ withdrawal rate |

*Table 3.1. Description of the two displacement modes used in simulations*

Before we investigate the effect of these simulation protocols, we describe the thermodynamic relations used to derive our discrete-domain model. In this model, the state of each compartment, $i$, is determined by its local wetting phase saturation, $S_i$.

From this we can assume that each compartment's free energy density, $f_i$, which is the Helmholtz free energy for the system in each compartment, is solely a function of the domain's local saturation, $f_i \equiv f_i(Si_i)$; Same goes for the Gibbs free energy of each compartment, $g_i \equiv g_i(s_i)$, which accounts for the free energy density in the pressure-controlled setting (Enderby, 1995). The total Helmholtz and Gibbs free energy of the system and the relation between them are as followed:

$$F = \sum F_i = \sum f_i(s_i)V_i \qquad \textit{(Eq. 10)}$$

$$G = \sum G_i = \sum g_i(s_i)V_i \qquad \textit{(Eq. 11)}$$

$$G = F + P_C V_w \qquad \textit{(Eq. 12)}$$

And so:

$$\sum(g_i(s_i)V_i) = \sum(f_i(s_i)V_i) + P_c V_w \qquad \textit{(Eq. 13)}$$

We are interested in minimizing the above equation with respect to the compartment saturations to determine the system's route to equilibrium, that is finding the solutions of $\frac{\partial G}{\partial s_i} = 0, i = 1, \dots, N$. Parameterizing this result in iteration time, we obtain the following evolution equations:

$$\frac{\partial s_i}{\partial t} = \frac{dg_i}{ds_i} = -\frac{df_i}{ds_i} - P_c\,, \qquad i = 1, \dots, N \qquad \textit{(Eq. 14)}$$

Note that it has been assumed that the above equation has been derived in a dimensionless form (by rescaling with a characteristic pressure for the cases we study) so that $f$ and $P_c$ do not represent physical units in this study.

When the system reaches the steady state, the saturation will not change with time, $\frac{\partial s_i}{\partial t} = 0$, and the condition for an equilibrium is satisfied, that is when $P_c = -\frac{df_i}{ds_i}$. The above equation is valid for both pressure-controlled and saturation-controlled displacements, however in the latter the capillary pressure becomes a Lagrange multiplier (for mathematical description of the Lagrange multiplier please refer to (Bertsekas, 1982 )) that is derived based on the constraint that the global wetting phase saturation, $S_w$, is constant. The global water saturation can be calculated as below:

$$S_w = \frac{V_w}{\sum V_i} = \frac{\sum V_{w,i}}{\sum V_i} = \frac{\sum (s_i V_i)}{\sum V_i} \qquad \textit{(Eq. 15)}$$

On the condition that the compartment pore volume, $V_i$, be constant for all the compartments, the derivation from equation 14, yields $\frac{\partial G}{\partial s_i} = (\frac{df_i}{ds_i} + P_c)V_i,\ i = 1, \dots, N$. Setting these equations to zero, we can eliminate $V_i$. Also, the global saturation, $S_w$, will be calculated by a simple arithmetic averaging, where $N$ is the total number of the compartments as previously indicated:

$$S_w = \frac{1}{N}\sum s_i \qquad \textit{(Eq. 16)}$$

However, if the compartment pore volume is not assumed to be equal throughout, the global saturation will be the volume-weighted average of the local saturations:

$$S_w = \frac{1}{\sum v_i} \sum s_i vi \qquad \textit{(Eq. 17)}$$

Moving on, in the saturation-controlled mode, to calculate the capillary pressure as a Lagrange multiplier, the global saturation constraint must hold at all times:

$$S_w = \frac{\sum (s_i V_i)}{\sum V_i} = constant \qquad \textit{(Eq. 18)}$$

Thus,

$$\frac{d}{dt} S_w = \frac{d}{dt} \frac{\sum (s_i V_i)}{\sum V_i} = \frac{1}{\sum V_i} \sum (\frac{\partial s_i}{\partial t} V_i) = 0 \qquad \textit{(Eq. 19)}$$

Inserting equation 14 into the above equation provides an expression for the Lagrange multiplier (or the capillary pressure) as in equation 21.

$$\sum (\frac{\partial s_i}{\partial t} V_i) = -\sum (\frac{df_i}{ds_i} V_i + P_c V_i) = 0 \qquad \textit{(Eq. 20)}$$

$$P_c = -\frac{\sum (V_i \frac{df_i}{ds_i})}{\sum V_i} \qquad \textit{(Eq. 21)}$$

The above expression is under the condition of unequal pore volumes. Otherwise, the Lagrange multiplier will be calculated again via an arithmetic averaging:

$$P_c = -\frac{\sum(\frac{df_i}{ds_i})}{N} \qquad \textit{(Eq. 22)}$$

For our discrete-domain model, we use a dimensionless, synthetic function to represent the compartment specific free energies, which introduces multiple discontinuous convex regions (or local minima) as the capillary pressure changes, that is where $\frac{\partial^2 f_i}{\partial s_i^2} \geq 0$, defining the multi-stability and metastability at equilibrium in each compartment. Whereas the resulting concave intervals between each equilibrium locus stand for the unstable states. This synthetic function consists of terms that explicates the reversible imbibition process and a term that demonstrates energy valleys and barriers. The function that we are referring to is as follows:

$$f_i^s = S_i\, log(S_i) + (1 - S_i)\, log(1 - S_i) - \omega_i S_i - C_i cos\,(K\pi S_i) \qquad \textit{(Eq. 23)}$$

Where $\omega_i$, characterize the strength of the wetting bias which is proportional to the difference between fluid-solid interfacial energies for the two fluids. A constant value for $\omega_i$ among the compartments means uniform wetting states throughout the system, while heterogeneous wetting states can be achieved by letting $\omega_i$ vary with compartments. In the last term of the function (the oscillatory term), the coefficients $C_i$ define the characteristic height of the barriers between energy valleys, while the parameter *K* signifies the frequency of oscillations (in essence the number of valleys)

in the energy functions. The implementation of the discrete-domain method for the investigation of the rugged energy landscapes and capillary hysteresis has been provided in MATLAB by my supervisor, Dr. Johan Olav Helland. The code has a main simulation loop that uses an iteration method that works based on the derivative of the synthetic energy function. The purpose of this study is to look into the different input parameters of the free energy density function and observe how their alterations affect the results of the simulation. Modifications were required in the code's script as well as the values and intervals of the input parameters for convergence purposes. Two main cases have been investigated:

i. Equal pore volume for the compartments
ii. Unequal pore volume for the compartments

For each case the simulations have been run based on both pressure-controlled and saturation-controlled protocols. The results consist of generally three diagrams as named below and have been provided and discussed in the next chapter:

1. The free energy density vs. compartment saturation plot: $f_i - S_{wi}$
2. The capillary pressure vs. global saturation plot: $P_c - S_w$
3. The compartment saturation vs. global saturation plot: $S_{wi} - S_w$

# Chapter 4. Results and Discussion

In this section the results from the simulations of the two aforementioned cases will be presented and discussed.

The simulations are run for a constant number of compartments, and the purpose is only to observe the behaviour of the discrete-domain model when variations are applied to the free energy density function's input parameters, as well as to the porosity of the compartments by the introduction of a pore volume parameter.

It is worth mentioning that apart from the number of compartments, the values assigned to these parameters are chosen with the sole purpose of showing the qualitative behaviour of the model with regards to the subject of discussion, i.e., hysteresis, and are therefore, not a precise quantitative assessment. This has been possible since the free energy density function provided in this study is provided in a dimensionless form. The following are the obtained results of our simulation attempts.

## 4. 1. Equal pore volume for the compartments

For the first case as mentioned before we consider discretization of the core-scale REV into a constant number of compartments, e.g., ten compartments. Also, note that the parameter *K* throughout *all* of the simulations is considered to be constant and equal to 8, which is an indicator of a constant number of valleys in the rugged energy landscape of the free energy density function:

- N_comp=10
- K=8

The simulations that were carried out in case 1 have been summarized in the chart below.

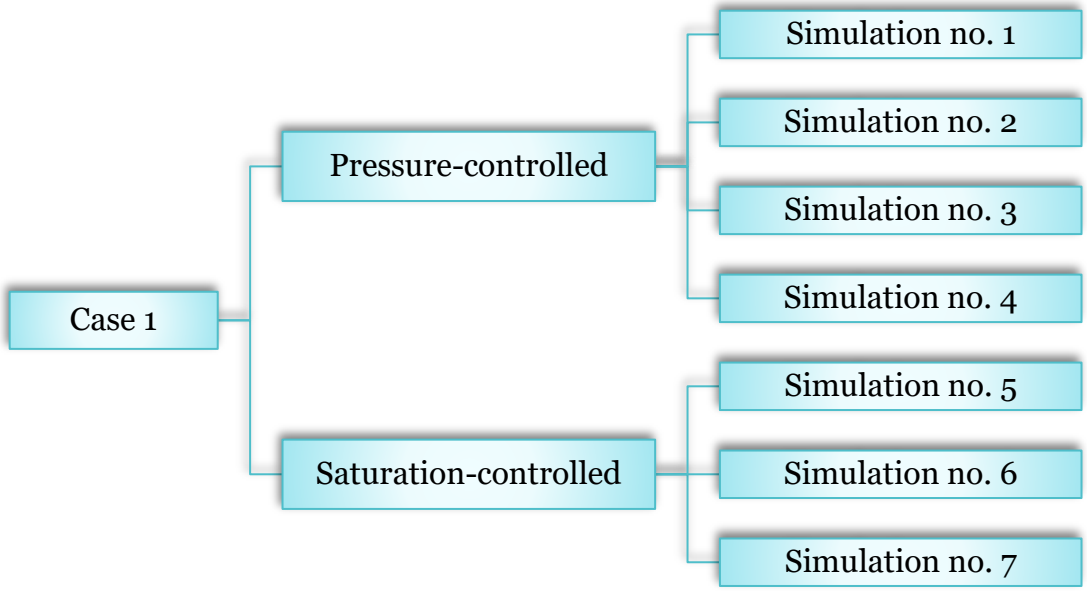


*Figure 4.1. The simulation runs from case 1*

### 4. 1. 1. Simulation no. 1

- $Ci = [0.01: 0.2]$ – Increasing with equal increments
- $\omega i = 6$ – Constant for all compartments

As mentioned, the input parameter of the free energy density function, *Ci*, defines the characteristic height of the energy barriers. In other words, it determines the height of the oscillations in the free energy density function.

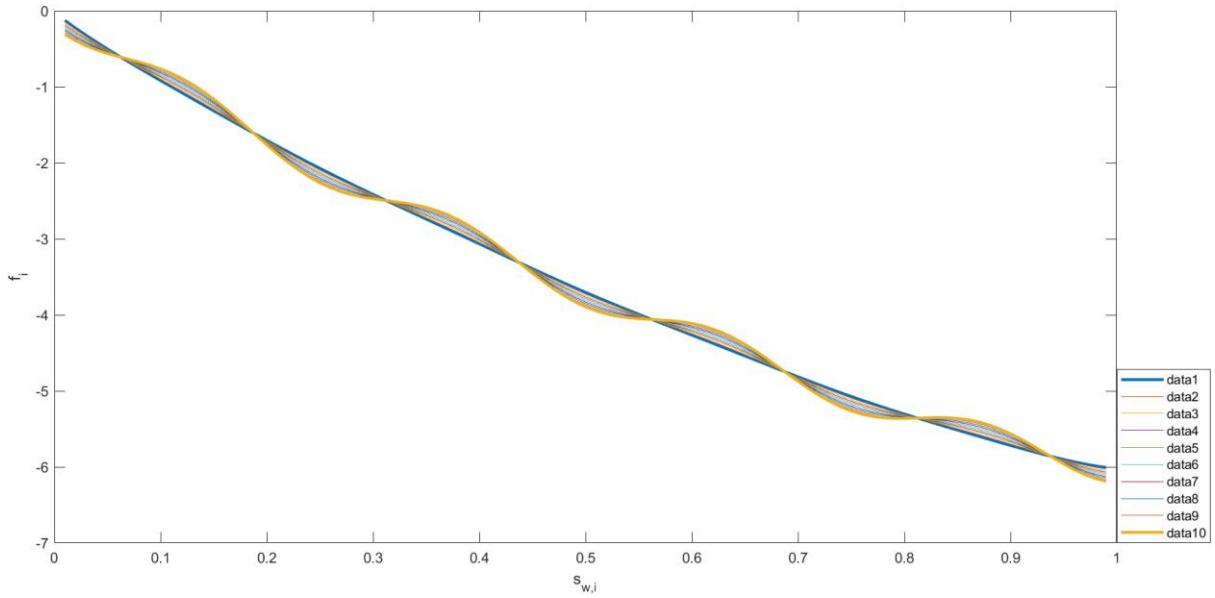


*Figure 4.2. The free energy density vs. compartment saturation diagram for the ten compartments in simulation no. 1; According to the legend the corresponding diagram of each of the compartments is displayed by a distinct colour, e.g., data1 shows the diagram belonging to the first compartment*

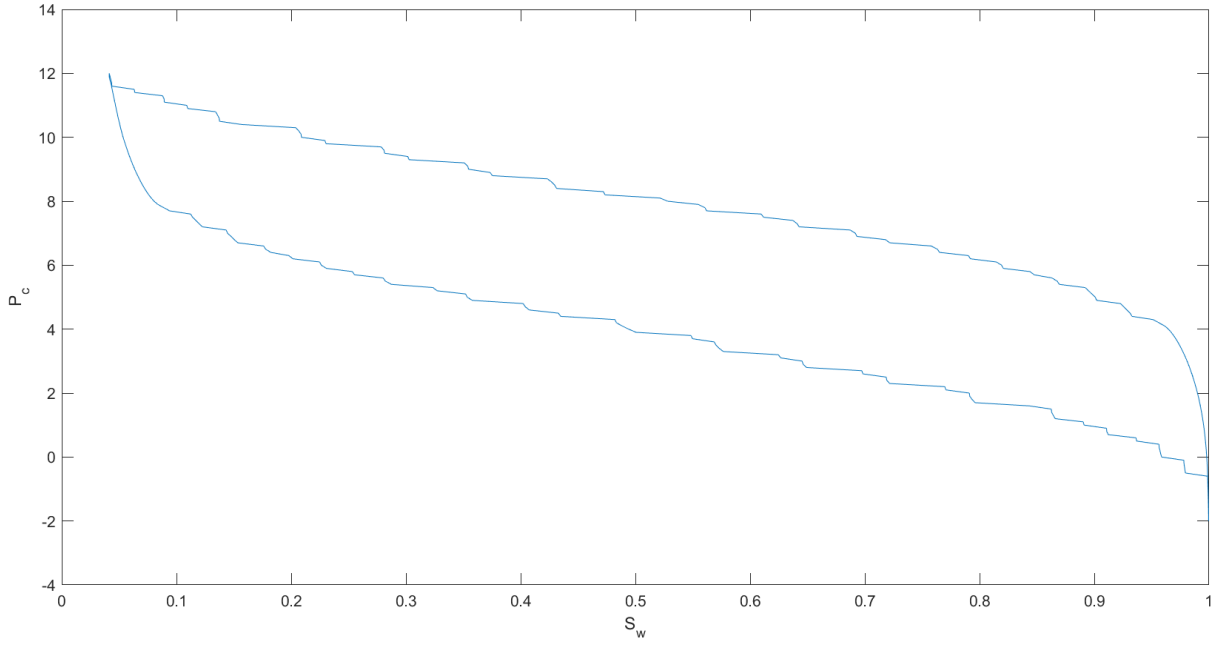


*Figure 4.3. The corresponding diagram of the capillary pressure as a function of the global saturation during drainage and imbibition in simulation no. 1*

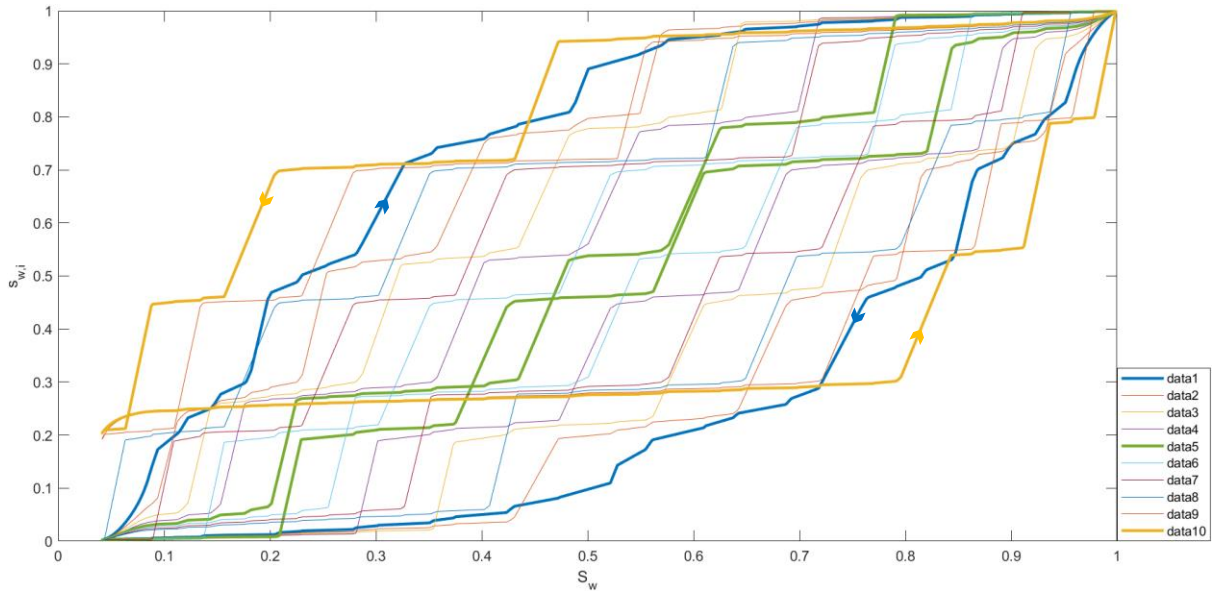


*Figure 4.4. The corresponding compartment- vs. global saturation diagram for the ten compartments in simulation no. 1, the drainage and imbibition curves are determined with arrows. The larger gap between the drainage and imbibition curves for one compartment represent bigger hysteresis whereas a narrower gap demonstrates smaller hysteresis in the two-way displacements.*

So, the higher the value of *Ci*, the more of a wavy-look the diagram gets and more significant barriers and fluctuations can be witnessed in the energy density function. This can be seen in figure 4.2, going from the first compartment where *C1=0.01* to the tenth compartment where *C10=0.2*.

As the free energy density function, $f^s$, is dependent on the interfacial characteristics of the phases, most importantly the interfacial area between the fluid-fluid and fluid-solid phase combinations, the energy barrier parameter, *Ci*, contributes to this characterization by representing the resistance to displacement in the porous media.

For example, in the case where the compartments' pore volumes are considered equal, a higher *Ci* demonstrates displacements through

narrower pore throats and therefore higher resistance as the non-wetting fluid will require a larger external drive, in this case capillary pressure, to displace from one pore to the adjacent pores through narrow throats and evidently lesser interfacial areas, during drainage.

Figure 4.3 depicts the resulting drainage and imbibition pressure curves from this simulation. As can be seen, these curves have a stair-case form, where the horizontal steps represent the unstable states of the interface and the irreversible Haines jumps (in the energy function diagram that is where $\frac{\partial^2 f_i}{\partial S_i^2} < 0$) while the inclined curved steps represent the reversible interface transitions (the metastable equilibrium locus).

In figure 4.4, the corresponding compartment vs. global saturation diagrams of the drainage and imbibition processes for the ten compartments are provided. It seems that during the drainage phase, the compartments are invaded by the non-wetting gas consecutively from compartment no. 1 to compartment no. 10 with an increasing factor of energy barrier, meaning that less gas is able to invade the next compartment resulting in higher water saturations locally. Looking at the figure, we can see that water also invades during imbibition in order from compartment no. 1 to 10. This is the reason for hysteresis in the compartment saturation curves. If the invasion order was from 1 to 10 in gas invasion, and from 10 to 1 in imbibition, hysteresis would be minimal. We can see that for both the first and last compartments which have the lowest and highest $C$ values respectively, a remarkable hysteresis in drainage and imbibition diagrams is obtained.

Interestingly, the drainage and imbibition curves obtained from these *C* values have swapped places in terms of the magnitude of the local saturations during the processes. This can be justified the following way: Pore throats are barriers to displacement in drainage. In imbibition, water is sucked spontaneously into these throats, and then it is instead in the bigger pores that the interfaces stabilize. It can be concluded that in the compartment with a lower value of *C*, the water is more easily and so rapidly displaced and substituted with the gas during drainage, ending in lower local saturations for given global saturations, than in the compartment with higher value of *C*, where the gas displaces the water to a limited extent and in a much more delayed drainage process, resulting in much higher local saturations for the corresponding global saturations. Predictably the degree of hysteresis has dropped, in the middle compartment, which is highlighted in green, as the preceding discussion around the trends suggests that in the middle compartments, the drainage and imbibition curves meet. The same result was obtained using other intervals of *Ci* values.

### 4. 1. 2. Simulation no. 2

- $Ci = 0.01$ (Blue) – Constant for all compartments
- $Ci = 0.2$ (Red) – Constant for all compartments
- $\omega i = 6$ – Constant for all compartments

Another thing to investigate is the hysteretic manner of the capillary pressure curves when simulations are run for constant values of *Ci*.

Figure 4.5 depicts a comparison between two single values of the $C$ parameter, constant for all compartments. At very low numbers, ca. $C < 0.004$, the capillary pressure curves for both drainage and imbibition show a very small hysteresis while as the $C$ value gets higher the pressure curves get more distant from each other which demonstrates higher degrees of hysteresis as well as maintaining a stair-case shape.

Note that choosing a constant value of $C$ for all compartments lead to no hysteresis in the local versus global saturation curves which in reality is not the case.

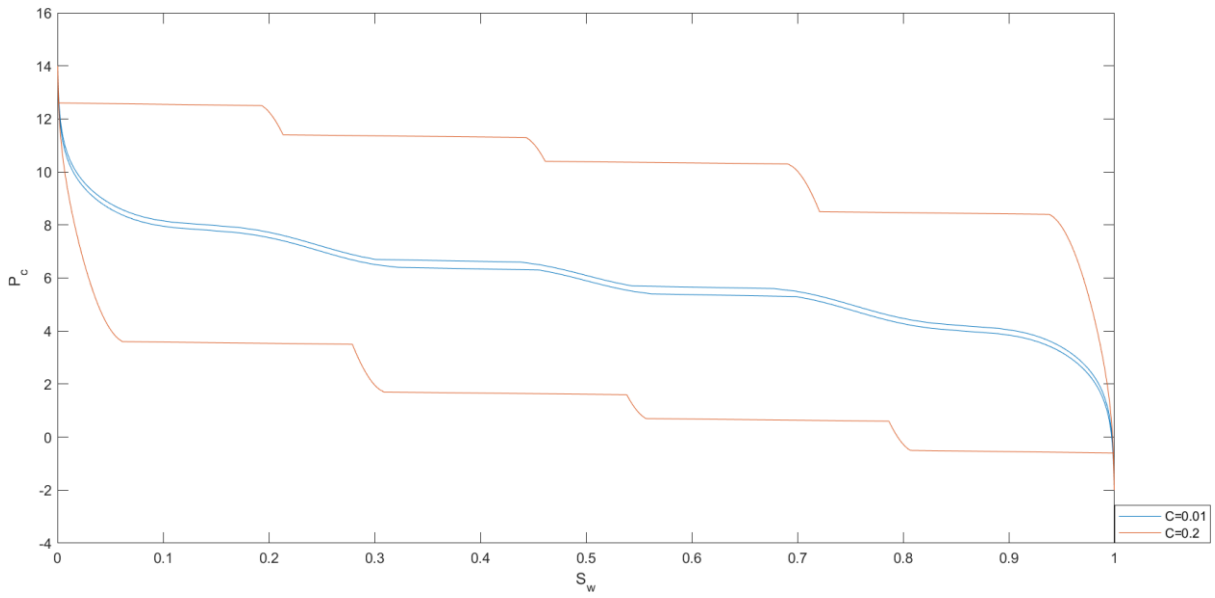


*Figure 4.5. The capillary pressure curves for two different, single values of the height of energy barrier, C=0.01 (blue) and C=0.2 (red) in simulation no. 2. For both cases the $C_i$ parameter is assumed to be constant for all of the compartments*

### 4. 1. 3. Simulation no. 3

- $Ci = 0.1$ – Constant for all compartments

- $\omega i = [1:5]$ – Increasing with equal increments

The input parameter of the free energy density function, $\omega i$, refers to the to the wettability bias of the porous media, that is a representative measure of the tendency of the pores towards wetting by each of the flowing phases.

When $\omega i$ is constant for all compartments, as was the situation in the previous simulation attempt, it means that all compartments have a similar wetting bias by both the non-wetting and the wetting phases throughout the simulations, however, when the value of this parameter is not constant throughout the different compartments, it is a reference of either heterogeneous wetting states or mixed wettability in the system.

Note that a mixed-wet system is the one where fractions of pores, usually smaller pores are filled with the generally wetting phase, in this case water, and are therefore water-wet, while some other fractions of pores, often being the larger pores are wetted by the other phase, which in this study is the CO2 gas phase (taken from the Schlumberger Oilfield Glossary).

In this simulation attempt, the $Ci$ parameters have been assumed to hold a constant value for all of the compartments; As shown in figure 4.6, the energy barriers across the simulation for all compartments exhibit a similar height. However, the value for the wetting bias, $\omega i$, is increasing from the first compartment to the last. In our study, positive values for $\omega i$ demonstrate a water-wet reservoir (contact angle, $\theta < 90$), where the reservoir goes from weakly to strongly water-wet by an increase in the value of the parameter. A neutrally wetting situation is when $\omega i$ equals

zero at a compartment ($\theta = 90$), while negative values introduce mixed wettability in the system which suggests the existence of compartments where the water is the non-wetting phase and the gas the wetting one ($\theta > 90$). Of course, this requires adjustments in the other parameters' input values as well that will be investigated in the next simulations.

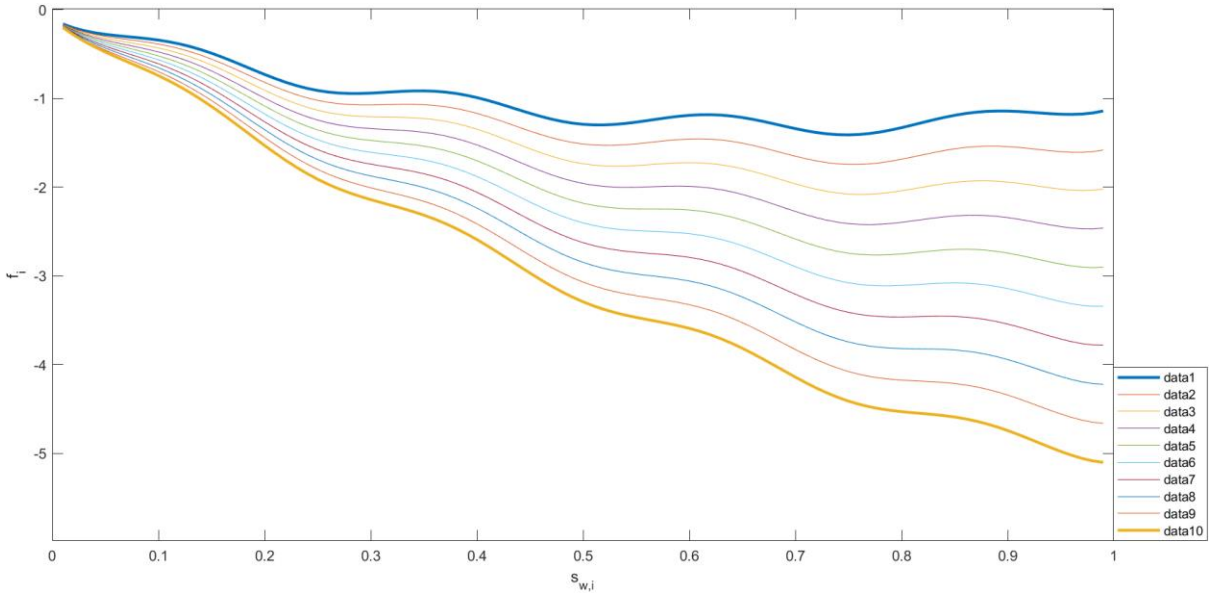


*Figure 4.6. The free energy density vs. compartment saturation diagram for the ten compartments in simulation no. 3*

The corresponding capillary pressure curves for the drainage and the imbibition processes is given in figure 4.7. In figure 4.8, it can be seen that the local- vs. the global saturation curves for all of the compartments exhibit a similar behaviour with low hysteresis degrees. Even though the hysteresis in the saturation diagram is small, it still persists in the

capillary pressure diagram. This can be appointed to the existence of the energy barriers and the fact that the *Ci* for all compartments is constant.

To our expectations, what can be clearly seen is that in the first compartment where $\omega$ is the lowest, the local saturations hold smaller values versus their corresponding global saturation, than in the last compartment where $\omega$ is the highest and therefore, the local saturations have higher values. Since the *Ci* parameter is constant, it is the $\omega i$ variations that make the energy function- and saturation curves different and give them the form they have. It is worth mentioning that in drainage, the gas invades compartments in the order from least water-wet to most water-wet in this case. On the contrary, during imbibition, water invades compartments in order from most water-wet to least water-wet.

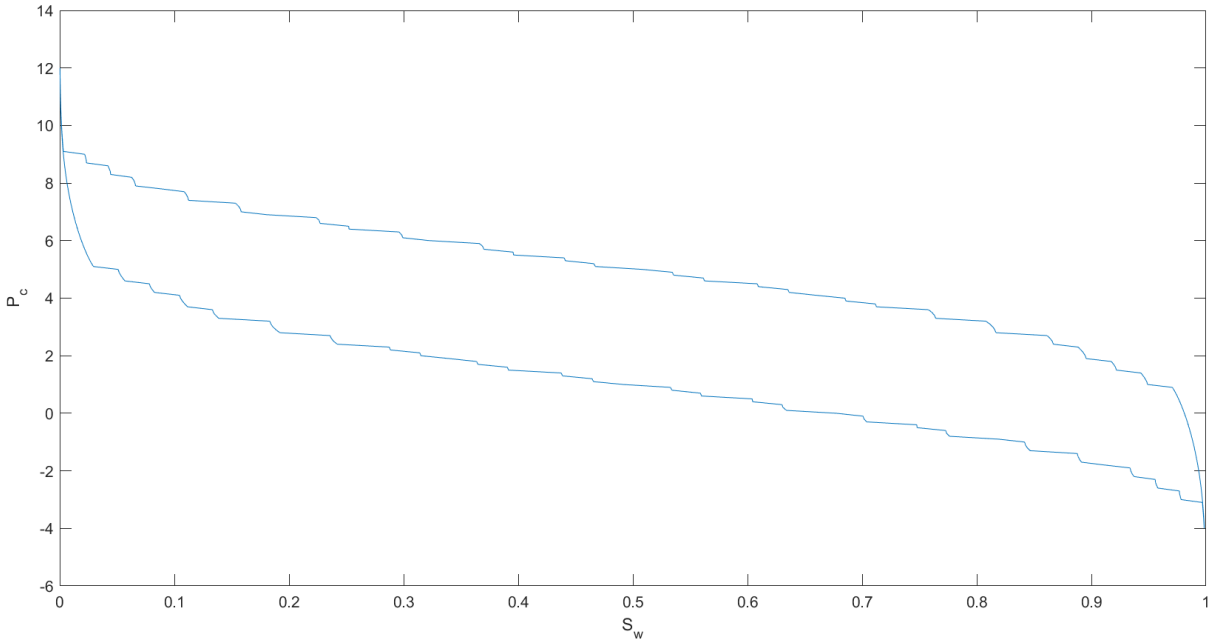


*Figure 4.7. The corresponding diagram of the capillary pressure as a function of the global saturation during drainage and imbibition in simulation no. 3*

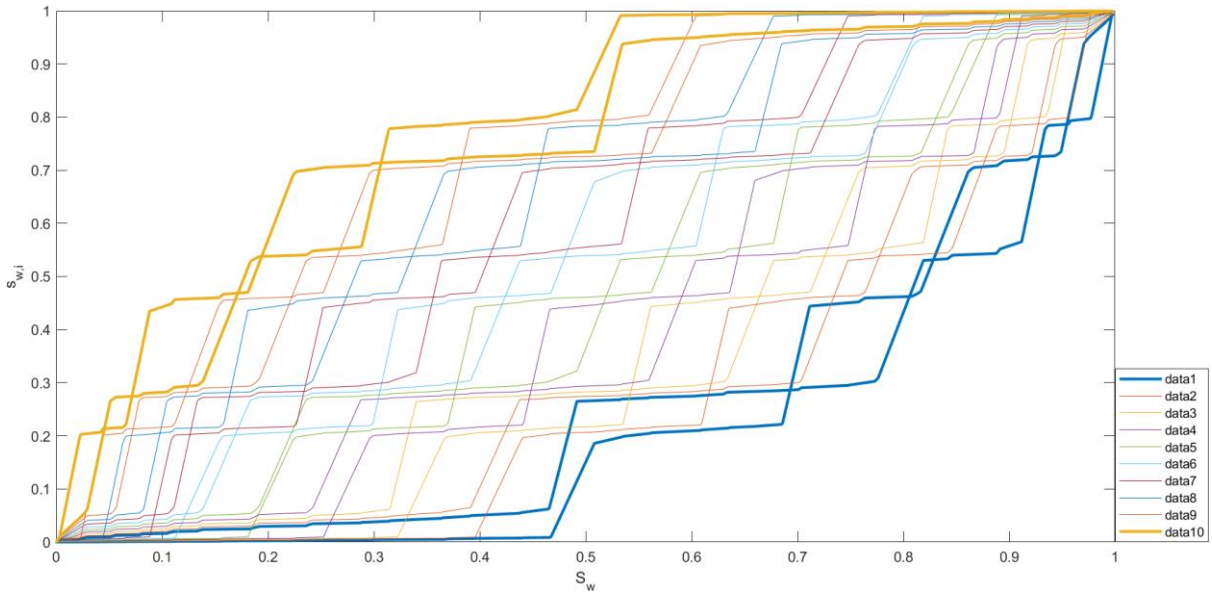


*Figure 4.8. The corresponding compartment- vs. global saturation diagram for the ten compartments in simulation no. 3*

### 4. 1. 4. Simulation no. 4

- $Ci = [-0.2: 0.2]$ – Increasing with equal increments
- $\omega i = [-3: 3]$ – Increasing with equal increments

The above is a relatively more realistic combination of parameters for the modelling of the displacements. The basis of the selection of the interval for $\omega i$ has been explained before, and the interval for $Ci$ has been adjusted accordingly in order for the simulation to converge.

Figure 4.9 clearly illustrates the way both parameters affect the energy density curves from the first to the last compartment. As expected, the lower the value of $Ci$ the less wavy of a look the curves get (data 5 and data 6), whereas the greater the input, the more substantial the energy

barriers become (the first and last curves). As for the wettability parameter, it can be seen that the change in the sign of the input (that is similar wetting strength but for the opposite phase) reverses the peaks and valleys. For instance, the convex regions of equilibrium in a strongly water-wet compartment, becomes the concave region of instability and irreversible Haines jumps if the compartment was strongly wetted by the $CO_2$ gas. Based on this logic and the previous discussions, the capillary pressure and saturation curves versus the global saturation can be explained.

The next series of simulations in this case will follow up same input settings under the saturation-controlled protocol.

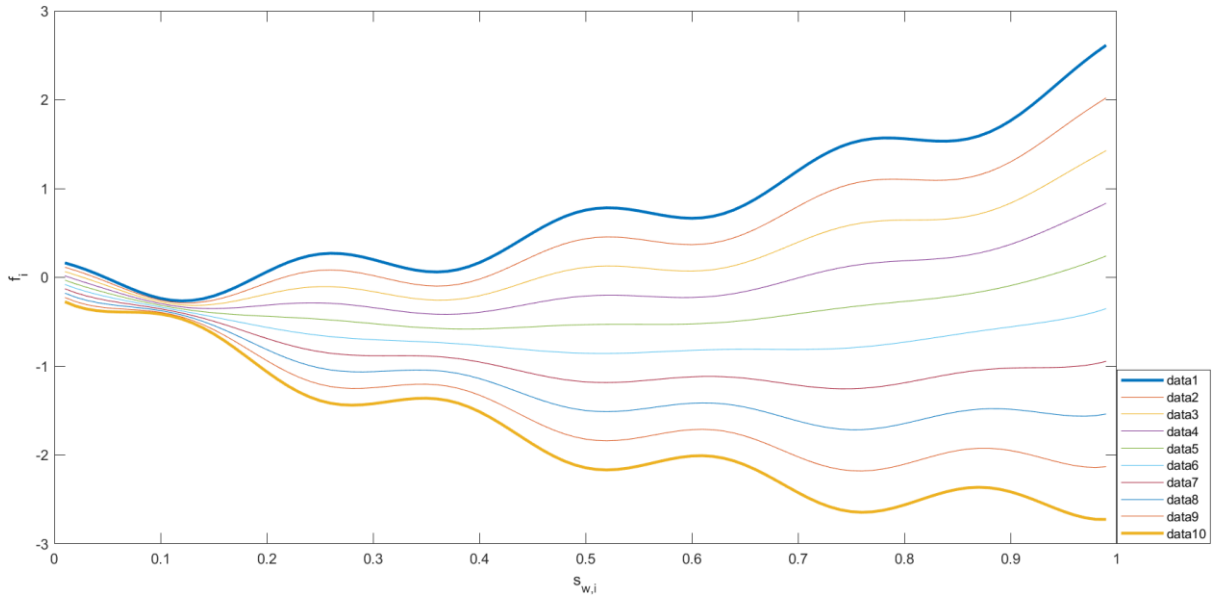


*Figure 4.9. The free energy density vs. compartment saturation diagram for the ten compartments in simulation no. 4*

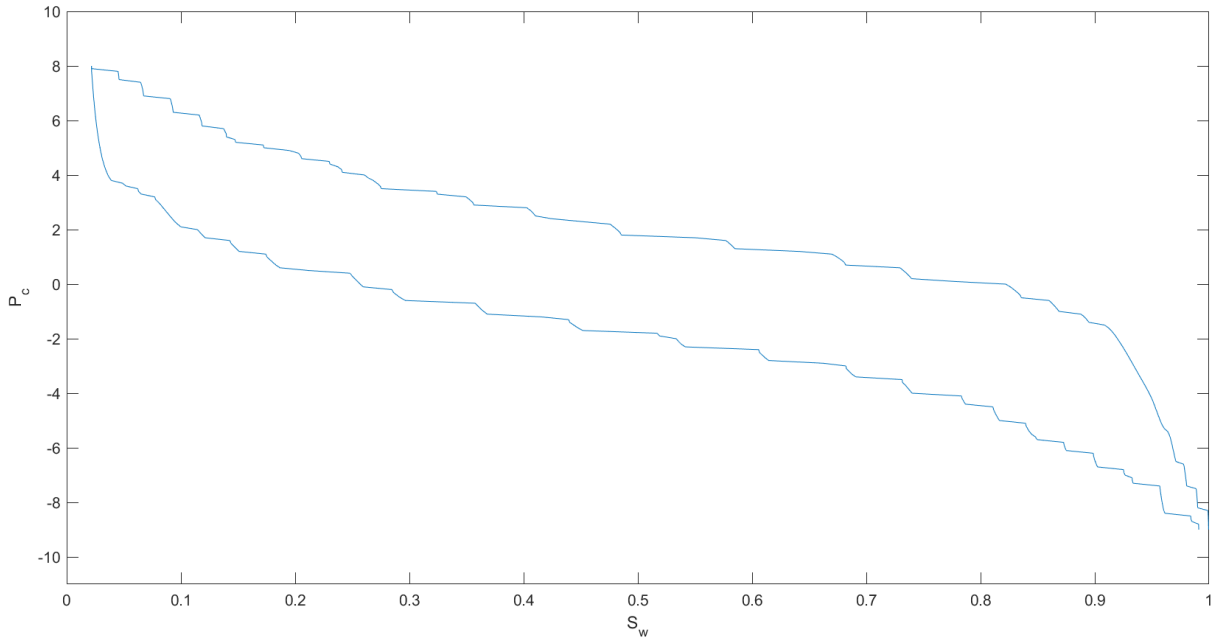


*Figure 4.10. The corresponding diagram of the capillary pressure as a function of the global saturation during drainage and imbibition in simulation no. 4*

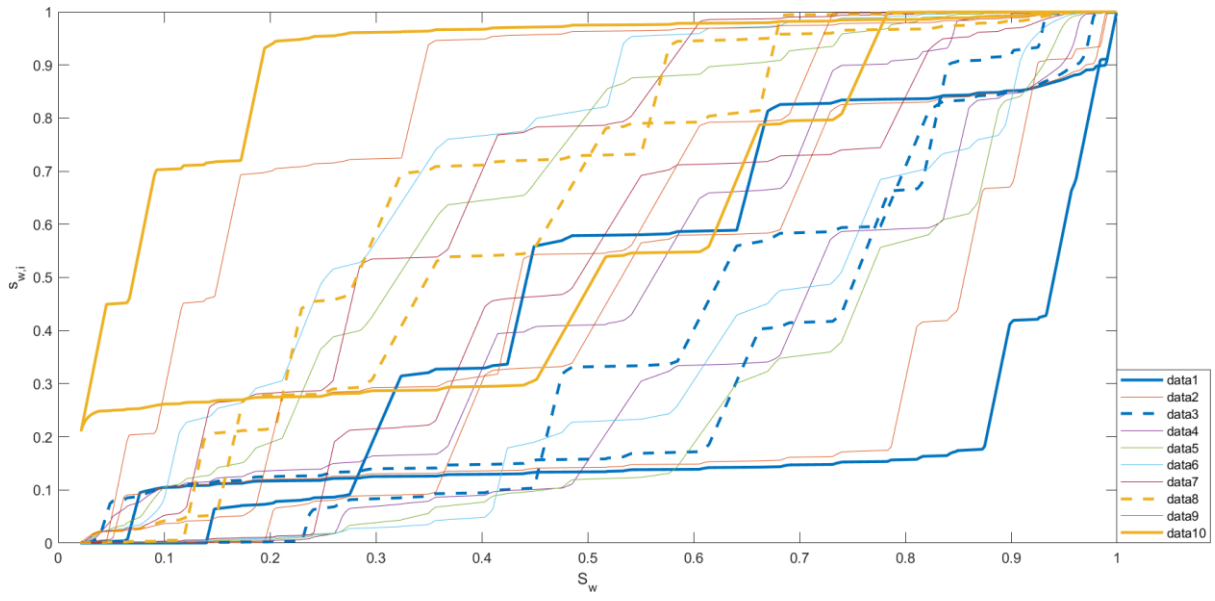


*Figure 4.11. The corresponding compartment- vs. global saturation diagram for the ten compartments in simulation no. 4*

### 4. 1. 5. Simulation no. 5

- $Ci = [0.01: 0.2]$ – Increasing with equal increments
- $\omega i = 6$ – Constant for all compartments

The first thing to remember in saturation-controlled simulations is that under same input conditions, the free energy density curves will be exactly the same as in the pressure-controlled runs. Nevertheless, the simulation of the capillary pressure and the saturation diagrams will depend on the simulation mode which affects the iterative loops that make up the model and are based on the energy derivatives.

The pressure curves for the drainage and imbibition processes for this simulation is provided in figure 4.12. As much as the trends are the same, the shape of the curves has changed into what is known as a "sawtooth structure". With this format, in the drainage curve, the peaking branches indicate the reversible displacements and the dropping branches, the Haines jumps, whereas, in the imbibition curve, the dropping valleys signify the smooth transitions and the rising branches, the irreversible jumps. A comparison between the capillary pressure curve in this simulation and that of the similar pressure-controlled simulation in simulation no.1, shows that the isons and rheons in both modes coincide which marks the accuracy of the model for implementation in both protocols. The same non-monotonic structure can be seen in the saturation curves (Johan Olav Helland et al., 2021). The discussion around the observed hysteresis in the pressure and local saturation curves based on value of the parameters in each compartment obeys the

same argumentation as for the pressure-controlled simulation. That said for the rest of the saturation-controlled simulation attempts, only the obtained diagrams have been presented without further discussion.

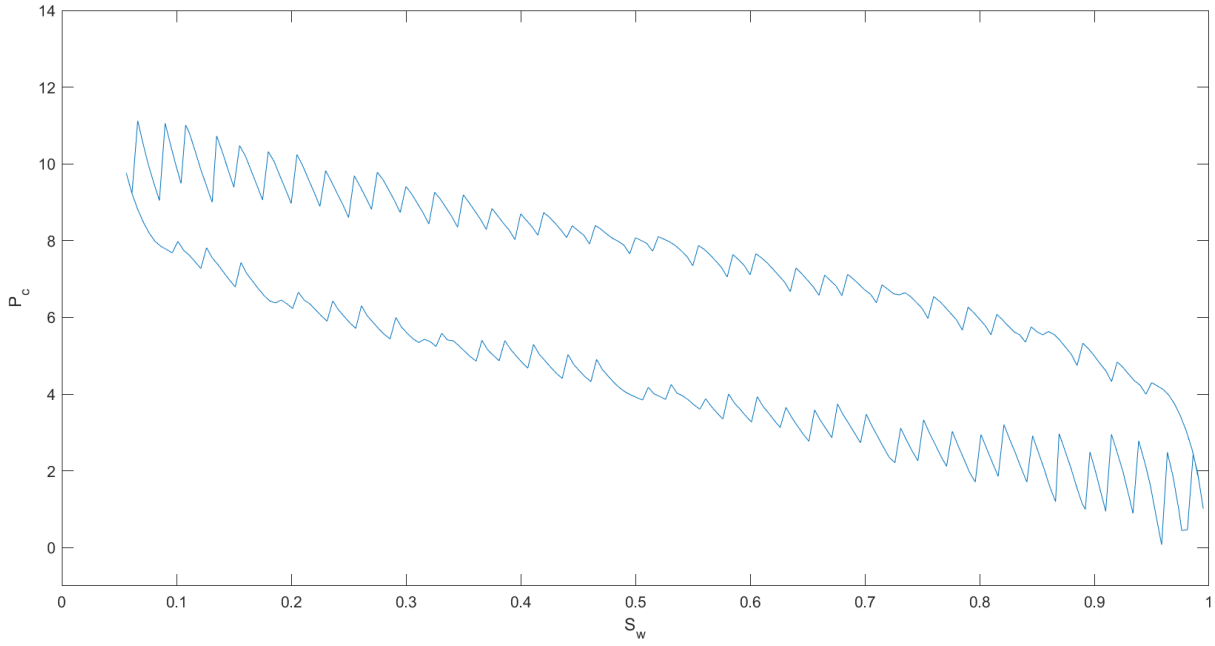


*Figure 4.12. The corresponding diagram of the capillary pressure as a function of the global saturation during drainage and imbibition in simulation no. 5*

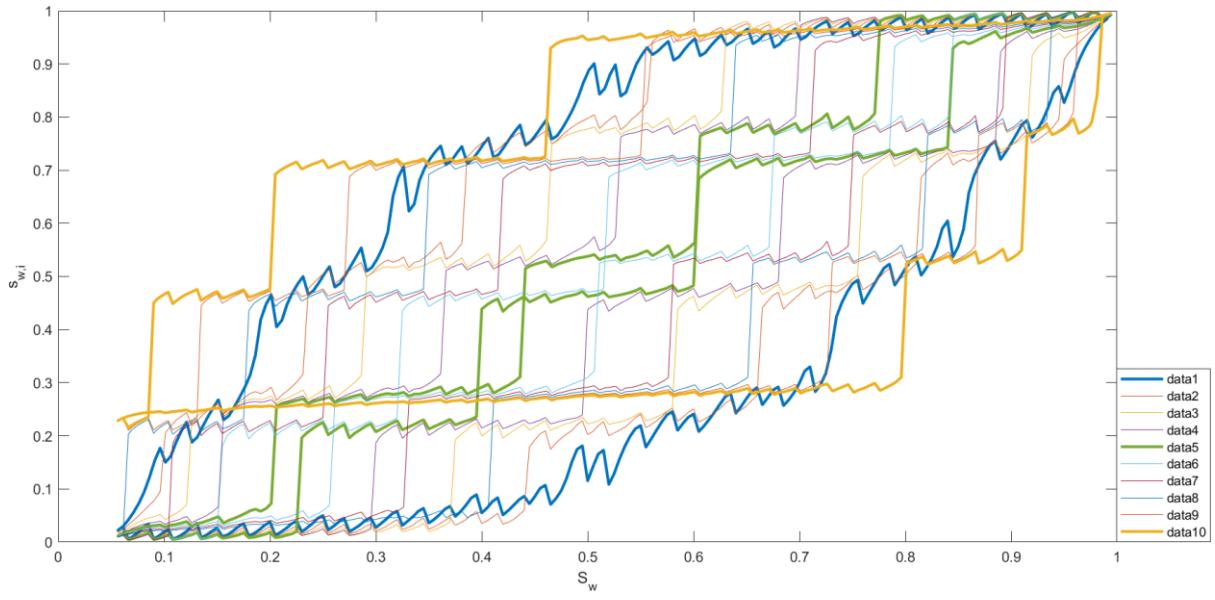


*Figure 4.13. The corresponding compartment- vs. global saturation diagram for the ten compartments in simulation no. 5*

### 4. 1. 6. Simulation no. 6

- $Ci = 0.1$ – Constant for all compartments
- $\omega i = [1:5]$ – Increasing with equal increments

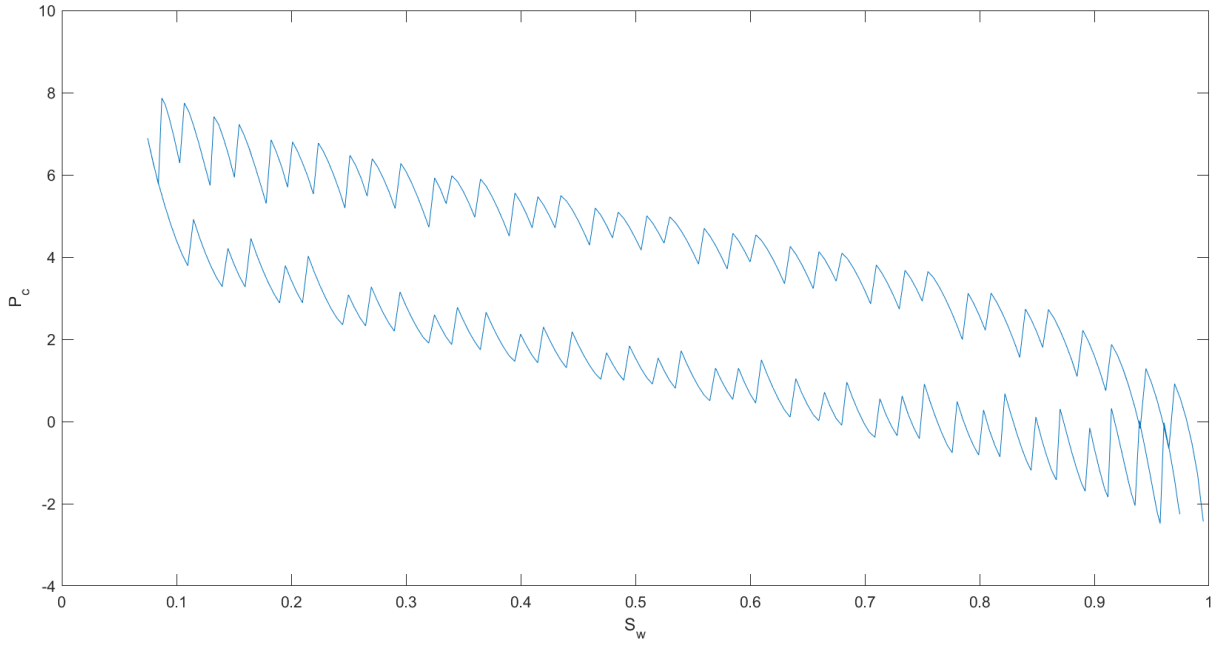


*Figure 4.14. The corresponding diagram of the capillary pressure as a function of the global saturation during drainage and imbibition in simulation no. 6*

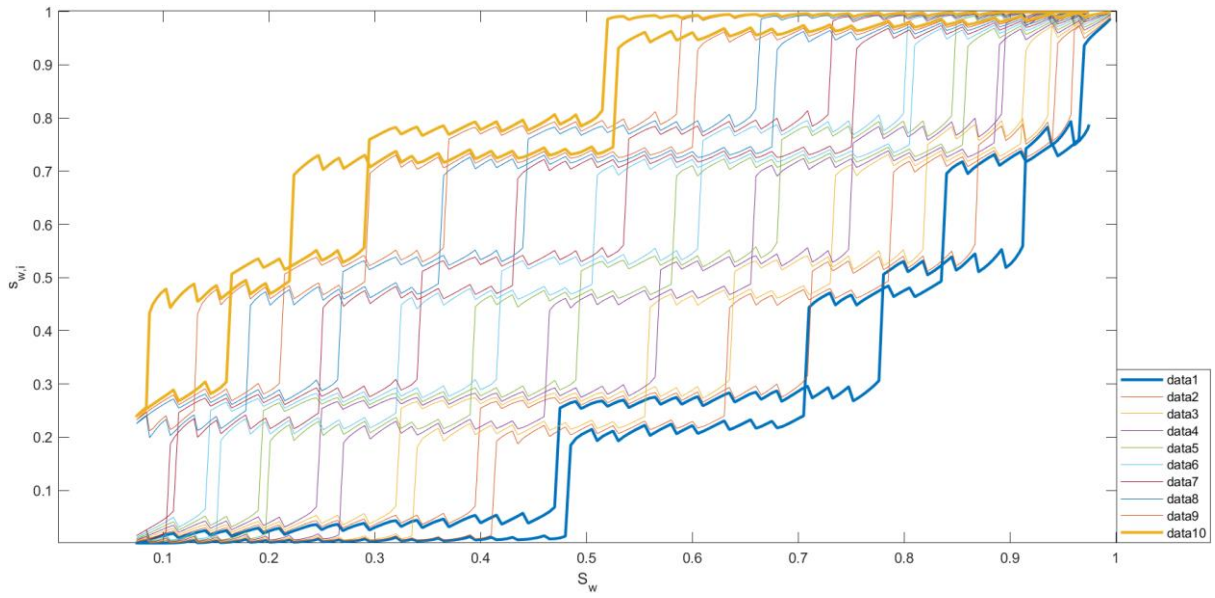


*Figure 4.15. The corresponding compartment- vs. global saturation diagram for the ten compartments in simulation no. 6*

### 4. 1. 7. Simulation no. 7

- $Ci = [-0.2: 0.2]$ – Increasing with equal increments
- $\omega i = [-3: 3]$ – Increasing with equal increments

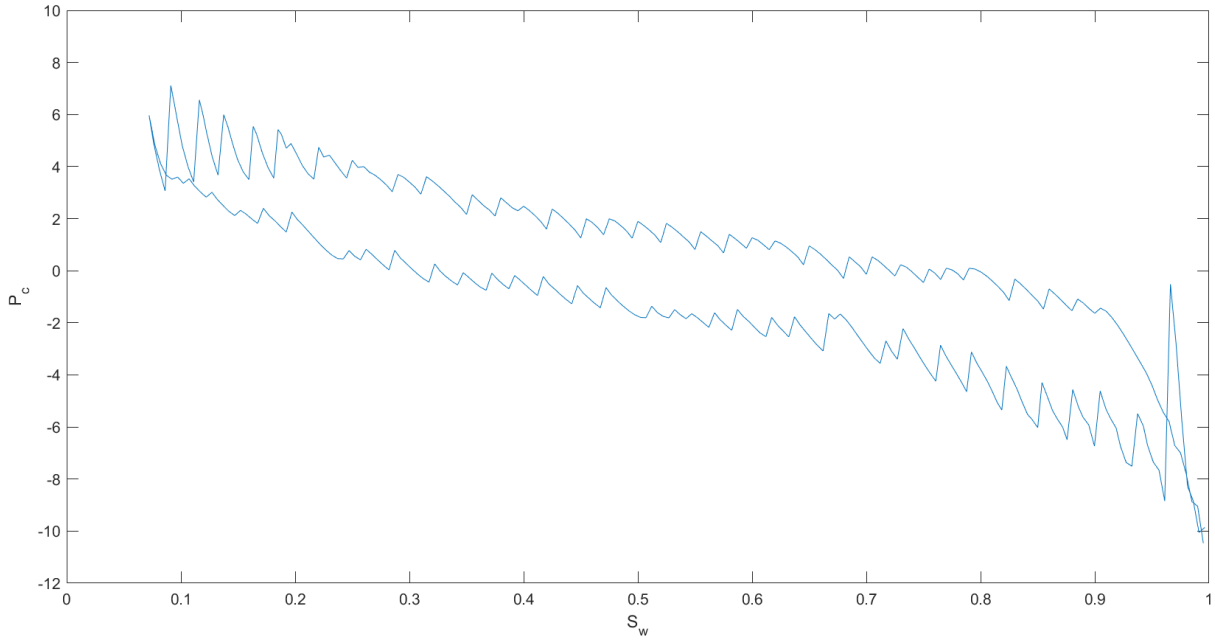


*Figure 4.16. The corresponding diagram of the capillary pressure as a function of the global saturation during drainage and imbibition in simulation no. 7*

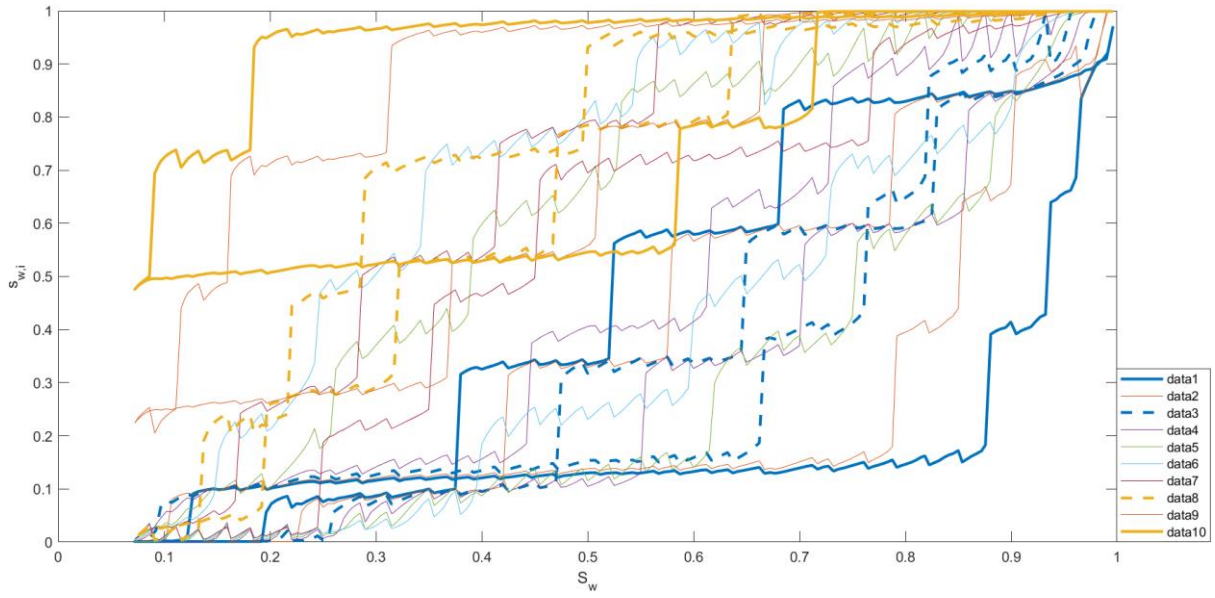


*Figure 4.17. The corresponding compartment- vs. global saturation diagram for the ten compartments in simulation no. 7*

## 4. 2. Unequal pore volume for the compartments

In this case we will run the same simulations as we did in the previous case but now, we will investigate the results for a varying compartment pore volume while all the other input parameters remain the same.

In order to account for non-uniform pore volumes, we have introduced the compartment pore volume as a new input parameter, *Vpi*, which in this case will be varying across the compartments as assigned in different attempts. Note that by assigning a single value to this parameter, no matter the input value, the simulations will occur according to the method explained in case 1. An assumption made in these simulations is that the fluid-fluid and fluid-solid interface areas which are two of the parameters that the energy density functions are composed of and therefore, *f*, are not affected by the varying compartment pore volumes as concluded from the simulation results.

In the cases where we assign an interval to the compartments' pore volumes, we investigate two conditions, one where the pore volume is increasing by the compartments and the other the contrary. We have added a new figure here that plots the variations of the energy barrier heights, if $Ci = [0.01: 0.2]$, with the compartment pore volume, Vpi, for an increasing interval of $Vpi = [0.5: 10]$ and a decreasing interval of $Vpi = [10: 0.5]$. See figure 4.19.

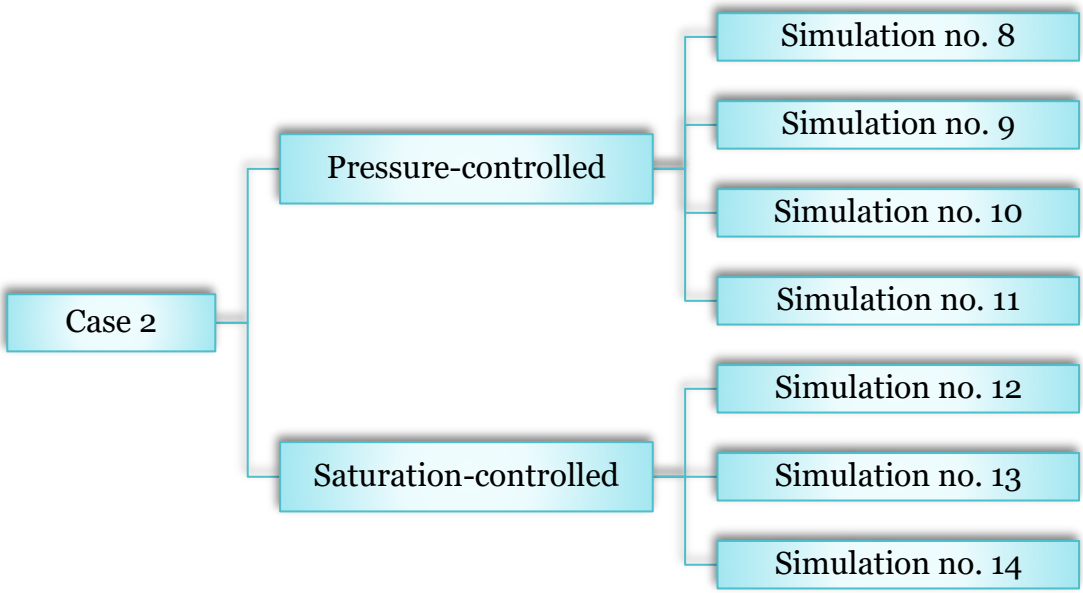


*Figure 4.18. Simulation runs for case 2*

### 4. 2. 1. Simulations no. 8 and 9

- $Ci = [0.01: 0.2]$ – Increasing with equal increments
- $\omega i = 6$ – Constant for all compartments
- Simulation no. 8:

  $Vpi = [0.5: 10]$ – Increasing with equal increments
- Simulation no. 9:

  $Vpi = [10: 0.5]$ – Decreasing with equal increments

Looking for the effect of the variations of compartment pore volumes, it can be seen in figures 4.20 and 4.21 respectively, that as *Vpi* increases with *Ci*, the hysteresis in the drainage and imbibition curves of the local

versus global saturation diagrams decreases and vice versa, meaning that a compartment with a smaller pore volume exhibits a much higher degree of hysteretic behaviour than a compartment with a larger pore volume.

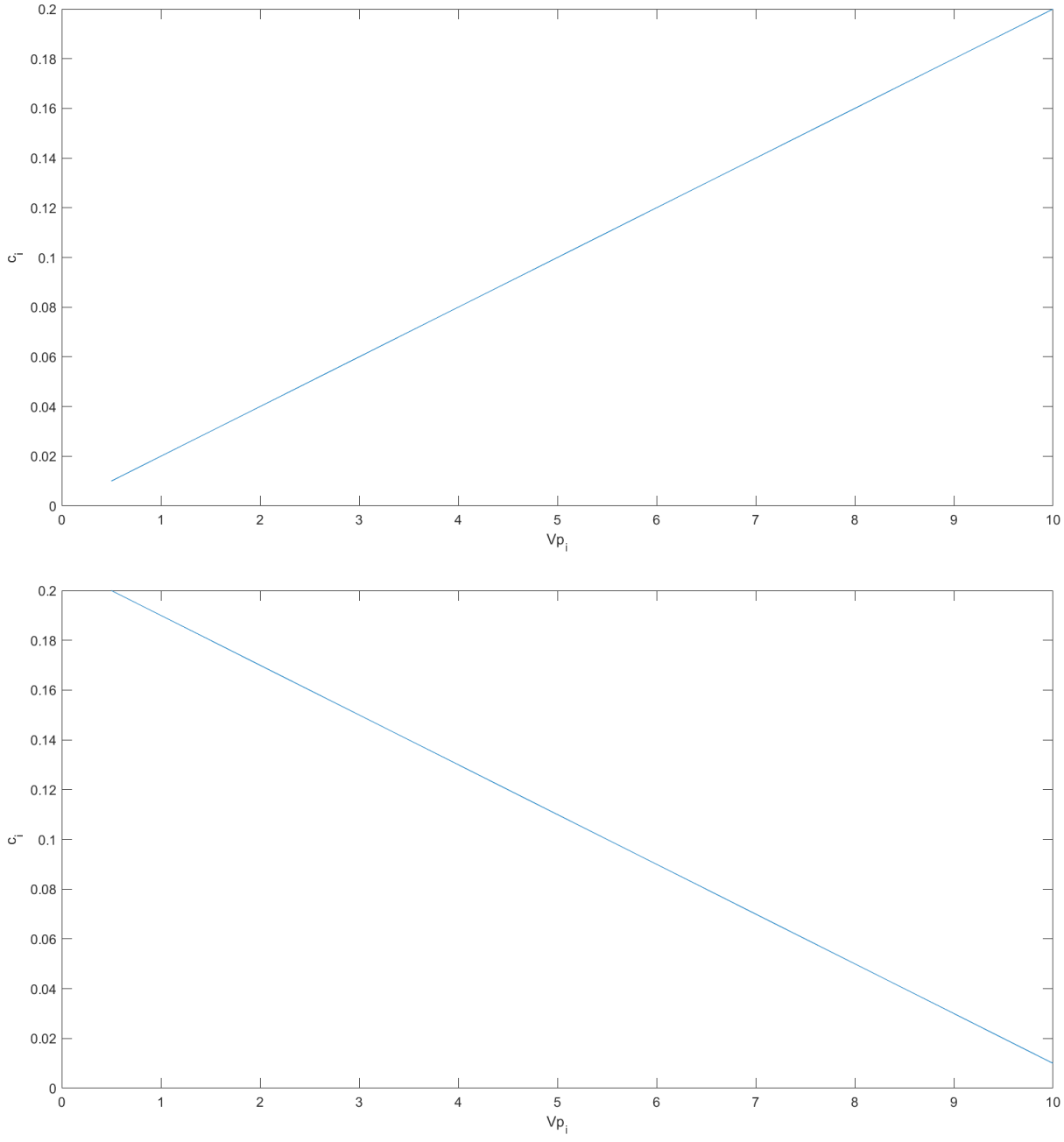


*Figure 4.19. Variations of the energy barrier height, Ci, with the compartment pore volume, Vpi*

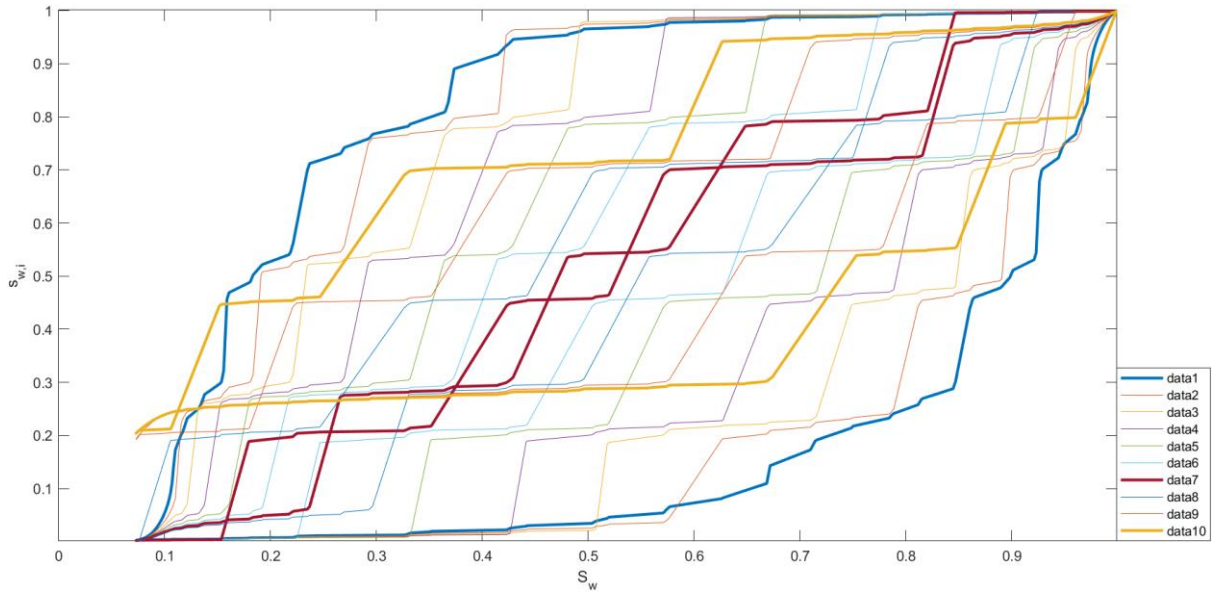


*Figure 4.20. The corresponding compartment- vs. global saturation diagram for the ten compartments in simulation no. 8*

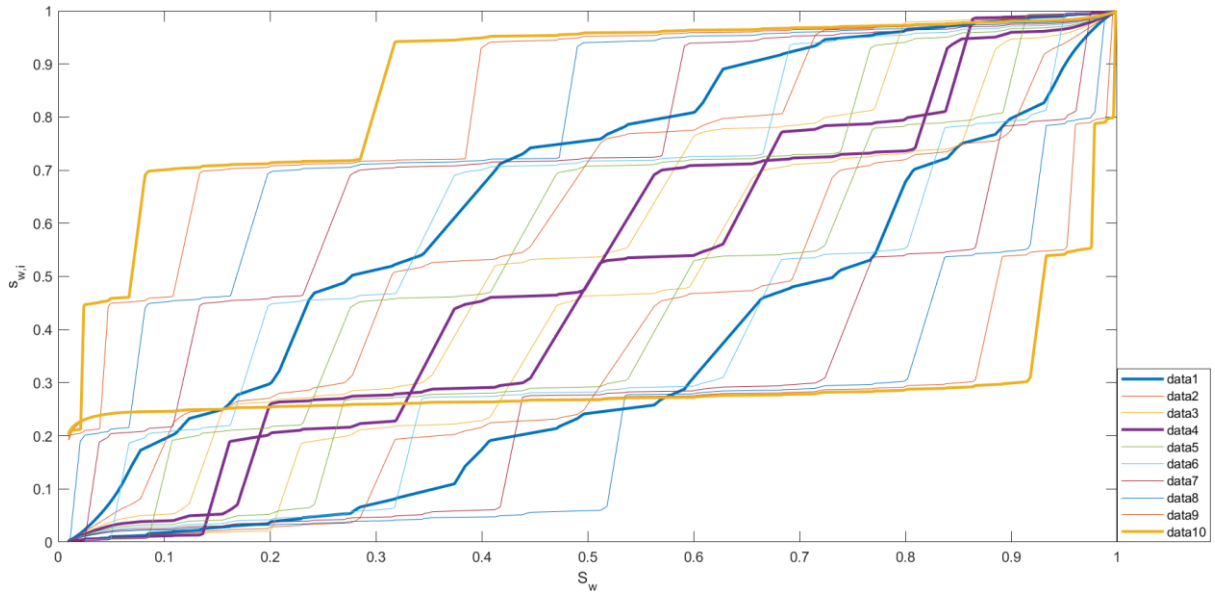


*Figure 4.21. The corresponding compartment- vs. global saturation diagram for the ten compartments in simulation no. 9*

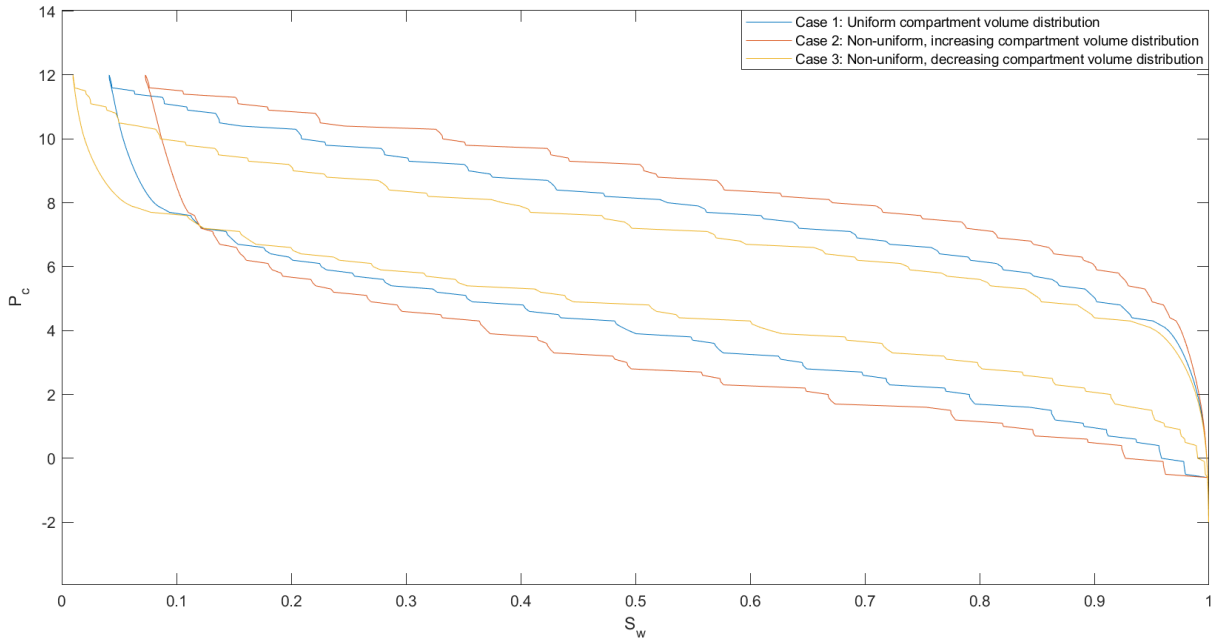


*Figure 4.22. The capillary pressure vs. global saturation curves for case 1 (simulation no. 1) with constant compartment pore volumes, case 2 (simulation no. 8) with increasing compartment pore volumes and case 3 (simulation no. 9) with decreasing compartment pore volumes; Note that the term "case" here does not refer to the main categorization of simulations, and its only purpose is to distinct the different diagrams*

Figure 4.22 shows a comparison between the capillary pressure curves for the conditions of constant (Simulation no. 1), increasing (Simulation no. 8) and decreasing (Simulation no. 9) compartment pore volumes.

It can be observed that compared to uniform pore volumes, an increasing interval of *Vpi* leads to a higher degree of hysteresis in the drainage and imbibition curves, while a decreasing interval ends in a lower degree. This can be due to the fact that at higher pore volumes, the chance of CO2 entrapment is higher, and so is the chance of the recurrence of the irreversibilities in the displacements. On the other hand, water flows smoothly into the smaller pores leading to less hysteresis. In addition, the larger the pore volume, the higher is the probability of the occurrence of a more intense Haines jump, which

clearly leads to higher hysteresis degree in the pressure curves. It can be argued that as the pore volume increases (with $C_i$), the ratio of the size of pores to the size of pore throats increases as well, enhancing the possibility of trapping as well as bigger Haines jumps.

### 4. 2. 2. Simulations no. 10 and 11

- $Ci = [-0.2: 0.2]$ – Increasing with equal increments
- $\omega i = [-3: 3]$ – Increasing with equal increments
- Simulation no.10:

  $Vpi = [0.5: 10]$ – Increasing with equal increments
- Simulation no. 11:

  $Vpi = [10: 0.5]$ – Decreasing with equal increments

In this simulation, it can be witnessed that the effect of the variations of the compartment pore volumes in general has been overshadowed by the changes in the wettability and energy barrier parameters to the point that by comparing figures 4.23 and 4.24, we can come to the same conclusion as in the first case. In other words, and to repeat ourselves, the wettability bias, $\omega i$, affects the outcome values of local saturations versus the global saturations and does not impact the evaluation of hysteresis in these diagrams, while on the contrary, the justification for the changes in the hysteretic manner in the different compartments can be appointed to energy barrier parameter, $Ci$.

As for the capillary pressure diagrams, it can be seen that compared to the situation where the pore volumes are equal, (which ends in curves

that have a homogeneous hysteresis degree for the saturation values throughout the drainage and imbibition processes), the capillary pressure curves exhibit higher hysteresis half-way through the processes. For the increasing pore volumes in simulation no. 9 this happens for lower global water saturations, whereas for the decreasing interval in simulation no. 10, this occurs for higher global water saturations (see figure 4.25). It can be argued that since both *Ci* and *ωi* vary, gas invasion will be a competition between the energy barrier and the wetting parameters. In simulation no. 9 for instance, the compartment with the smallest volume is invaded first, and the bigger volumes at the end. Therefore, we see bigger hysteresis gap on the pressure curves at low global saturations, while in simulation no. 10, the opposite is true (bigger hysteresis gap at high global saturation).

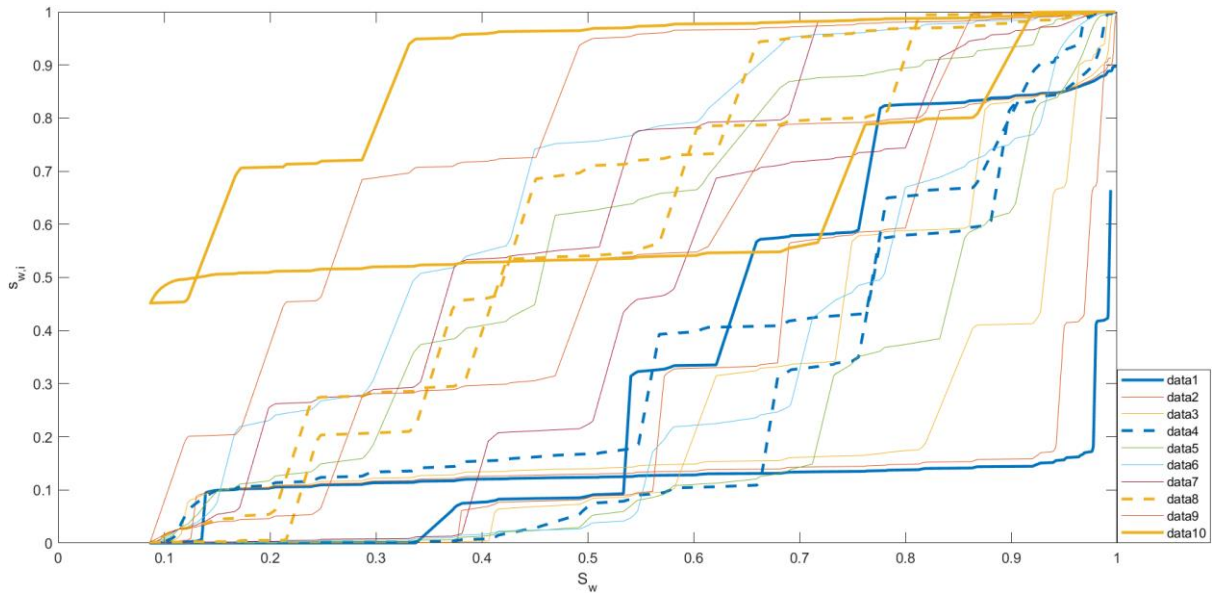


*Figure 4.23. The corresponding compartment- vs. global saturation diagram for the ten compartments in simulation no. 10*

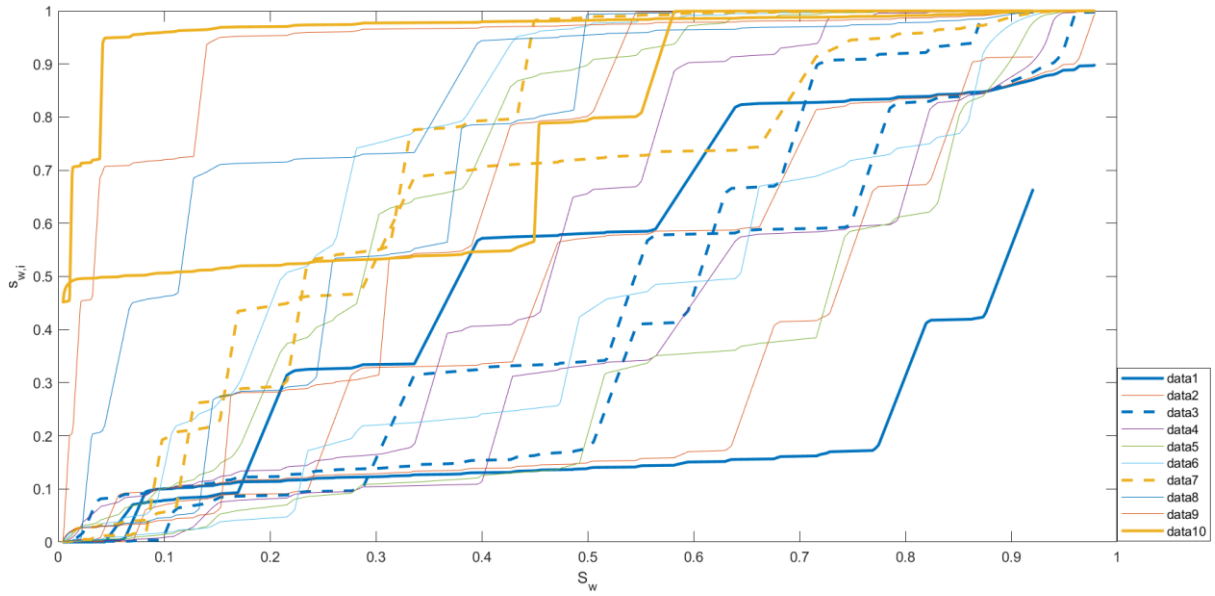


*Figure 4.24. The corresponding compartment- vs. global saturation diagram for the ten compartments in simulation no. 11*

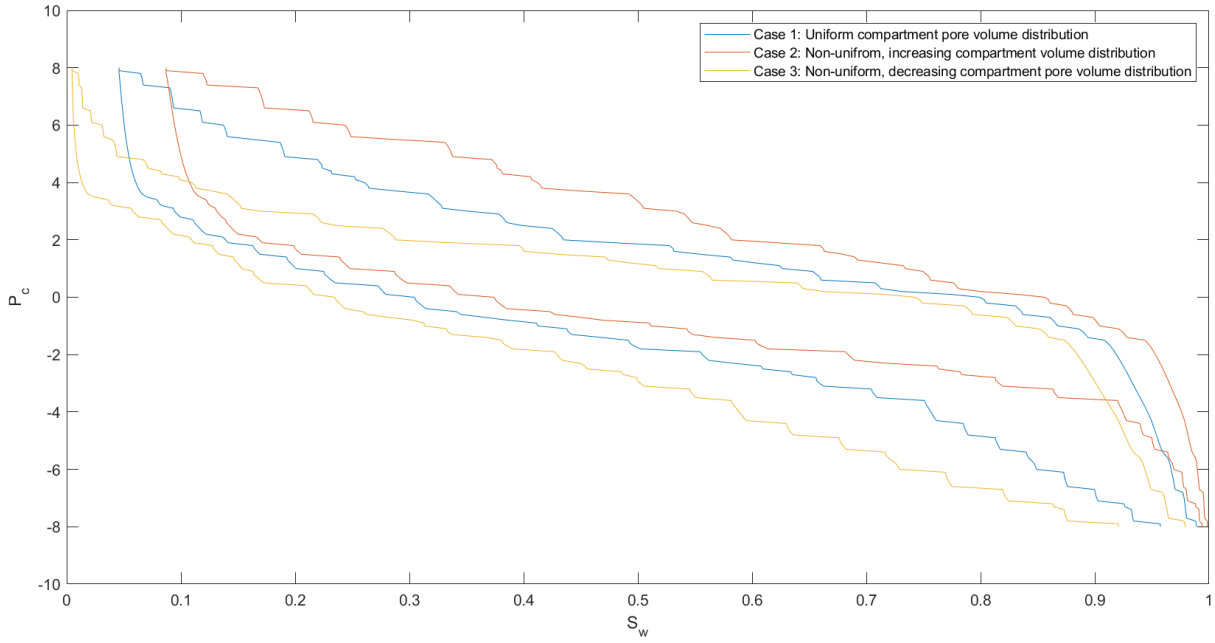


*Figure 4.25. The capillary pressure vs. global saturation curves for case 1 (simulation no. 4), case 2 (simulation no. 10) and case 3 (simulation no. 11)*

The next series of results are obtained from the saturation-controlled simulations in this case for which, from the results it can be observed that the same discussions as in the pressure-controlled attempts can be argued with the difference that the sawtooth structure in both capillary pressure and saturation diagrams is now back. Therefore, we refrain from further explanation for the following results.

### 4. 2. 3. Simulations no. 12 and 13

- $Ci = [0.01: 0.2]$ – Increasing with equal increments
- $\omega i = 6$ – Constant for all compartments
- Simulation no.12:

  $Vpi = [0.5: 10]$ – Increasing with equal increments
- Simulation no. 13:

  $Vpi = [10: 0.5]$ – Decreasing with equal increments

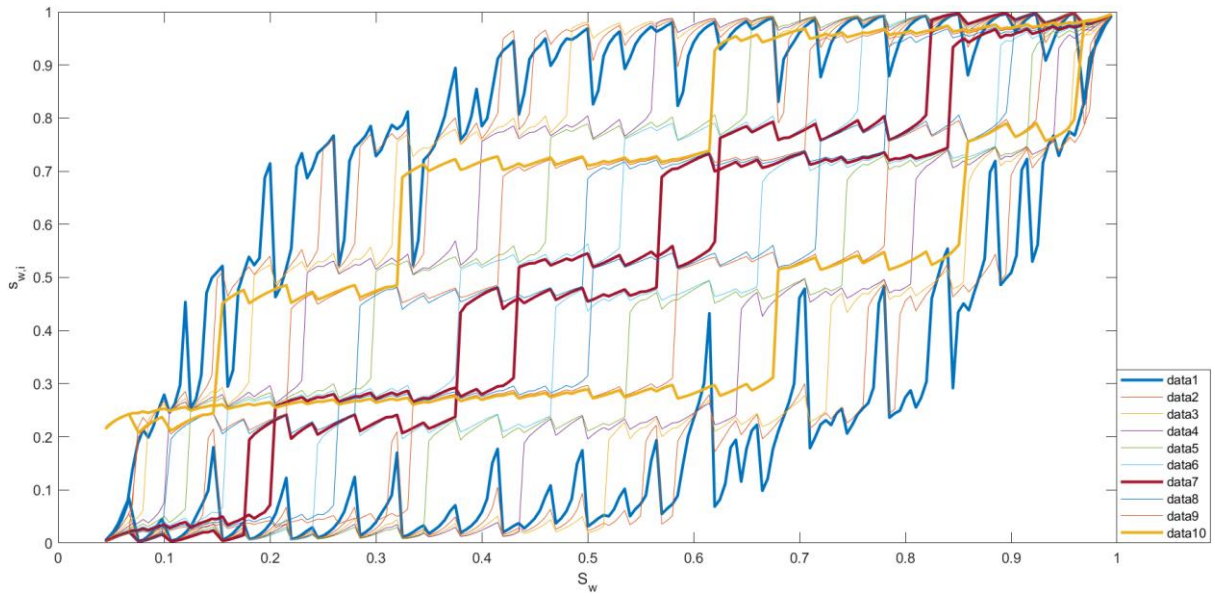

*Figure 4.26. The corresponding compartment- vs. global saturation diagram for the ten compartments in simulation no. 12*

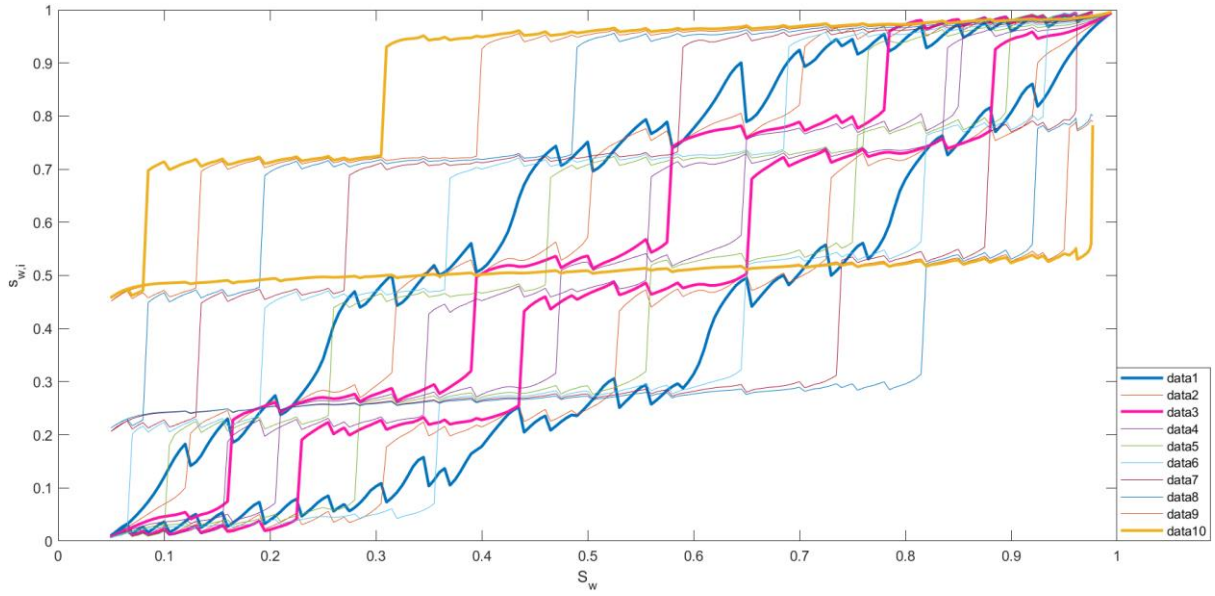


*Figure 4.27. The corresponding compartment- vs. global saturation diagram for the ten compartments in simulation no. 13*

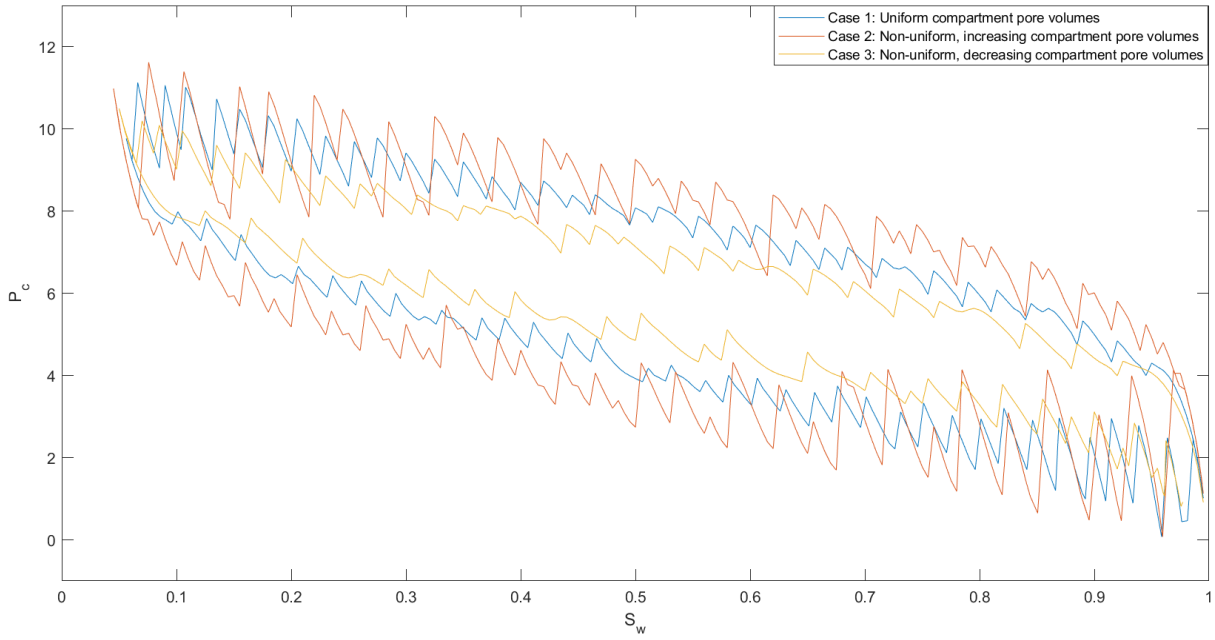


*Figure 4.28. The capillary pressure vs. global saturation curves for case 1 (simulation no. 5), case 2 (simulation no. 12) and case 3 (simulation no. 13)*

### 4. 2. 4. Simulations no. 14 and 15

- $Ci = [-0.2: 0.2]$ – Increasing with equal increments
- $\omega i = [-3: 3]$ – Constant for all compartments
- Simulation no.14:

  $Vpi = [0.5: 10]$ – Increasing with equal increments
- Simulation no. 15:

  $Vpi = [10: 0.5]$ – Decreasing with equal increments

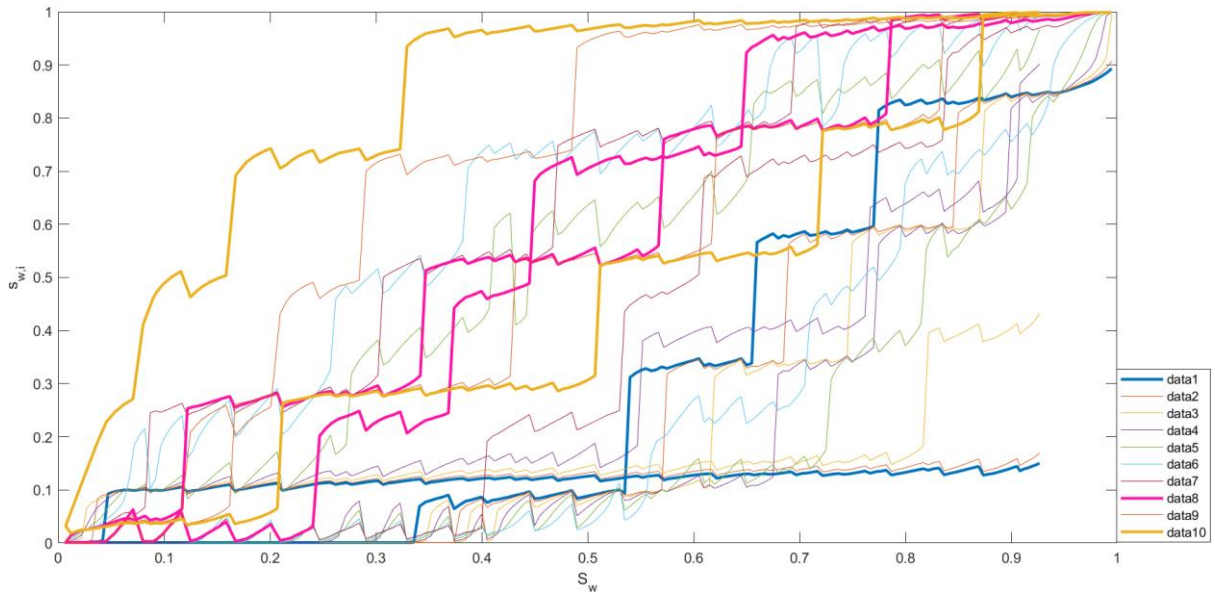


*Figure 4.29. The corresponding compartment- vs. global saturation diagram for the ten compartments in simulation no. 14*

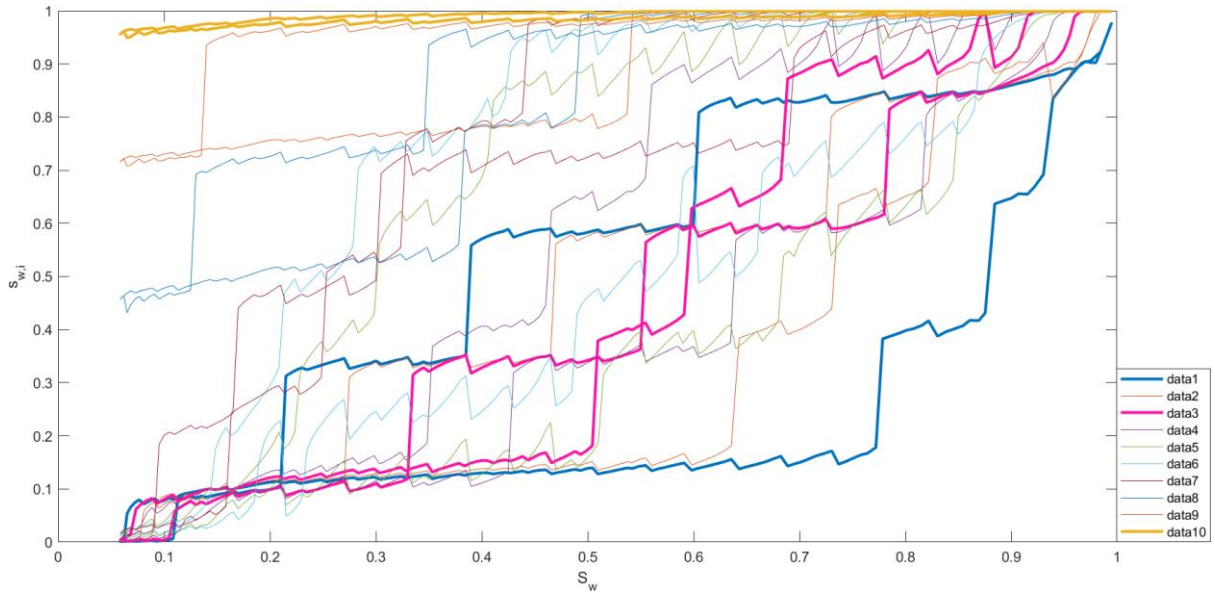


*Figure 4.30. The corresponding compartment- vs. global saturation diagram for the ten compartments in simulation no. 15*

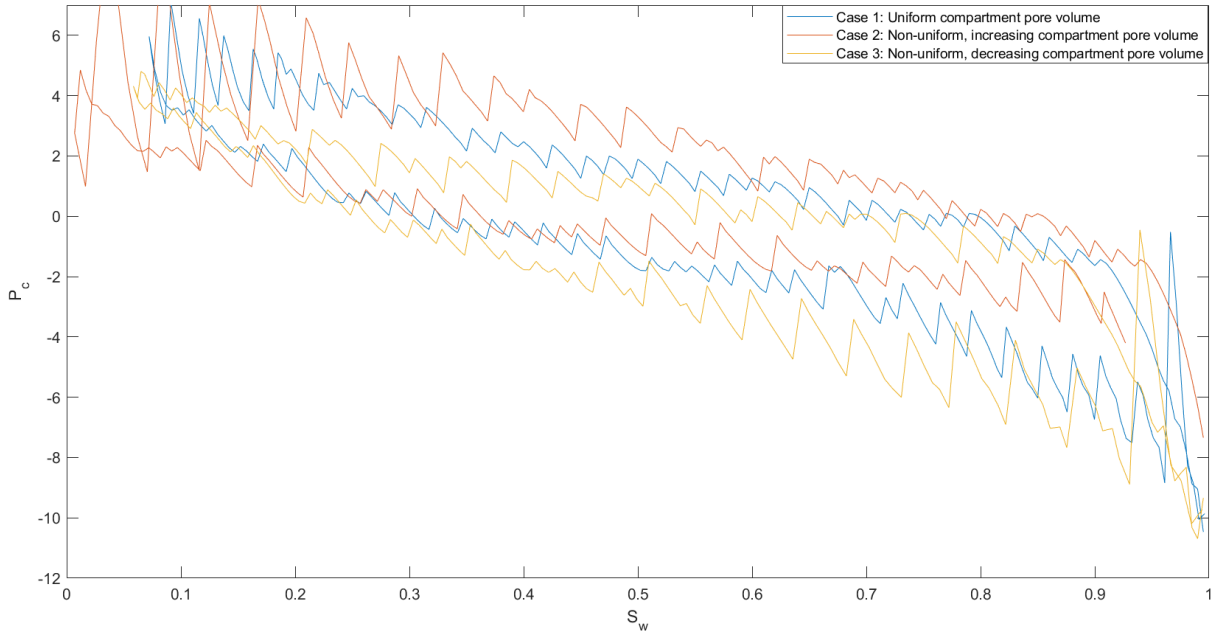


*Figure 4.31. The capillary pressure vs. global saturation curves for case 1 (simulation no. 7), case 2 (simulation no. 14) and case 3 (simulation no. 15)*

# Chapter 5. A suggestion for further investigation

There are quite many ways to look into the discrete-domain model that was used to simulate the two-phase displacements in this study. In this thesis the main purpose was to study the effects of the variations in the input parameters, as well as the introduction of the pore volume parameter to be able to account for the inequality in compartments' pore volumes. Another recommended path is to investigate the factor of upscaling, that is when the REV's discretization goes from a greater number to a smaller number of compartments and hence the model's validity will be examined for displacements at a larger scale. Of course, in order to do this, we need modifications within our discrete-domain model which will not be discussed here. As an instance, the results for the upscaling of our REV which is initially divided into twenty compartments, and then scaled up in two separate steps (upscaling from initially twenty compartments in each step) into ten and five compartments respectively has been provided in the following. Let us call it case 3. The rest of the conditions for this series of simulation attempts is the same as in simulation no. 1.

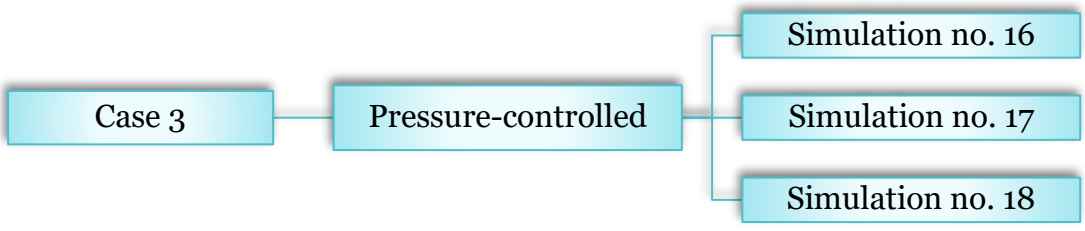


*Figure 5.1. Simulation runs considering upscaling*

## 5. 1. Upscaling with equal compartment pore volume

### 5. 1. 1. Simulations no. 16, 17 and 18

- $Ci = [0.01: 0.2]$ – Increasing with equal increments
- $\omega i = 6$ – Constant for all compartments
- Simulation no.16:

$$N_{comp} = 20$$

- Simulation no. 17:

$$N_{comp} = 10$$

- Simulation no. 18:

$$N_{comp} = 5$$

As it can be seen from the obtained plots, for the initial number of compartments, the results are exactly the same way as we expected and had seen in simulation no. 1. The behaviour of the system after both upscaling steps looks quite similar, in that, the form of the free energy density diagrams changes in a way that the concave regions of the diagram which used to represent the instabilities in the displacements, have now turned convex, joining the former equilibrium locus. The challenge here is that the coarse scale energy function is calculated based on fine-scale equilibrium states, so a big uncertainty, is if the energy barriers is described correctly. This can also impact the level of the pressure-saturation curves and explain why the fine scale and coarse scale curves sometimes could differ.

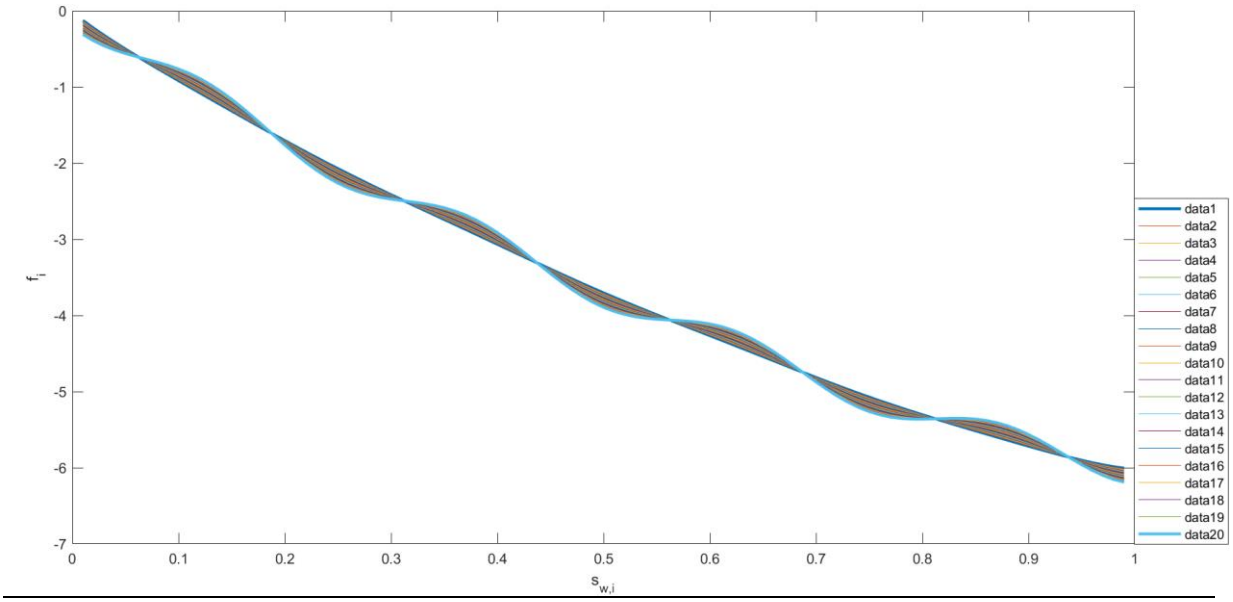


*Figure 5.2. The free energy density vs. compartment saturation diagram for the twenty compartments in simulation no. 16*

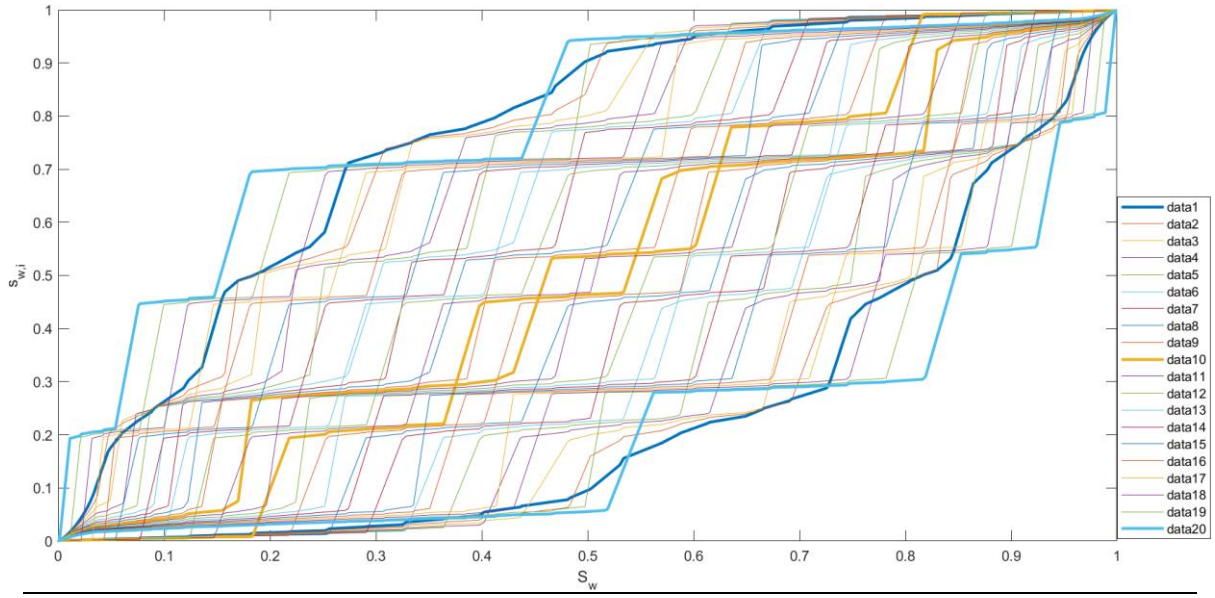


*Figure 5.3. The corresponding compartment- vs. global saturation diagram for the ten compartments in simulation no. 16*

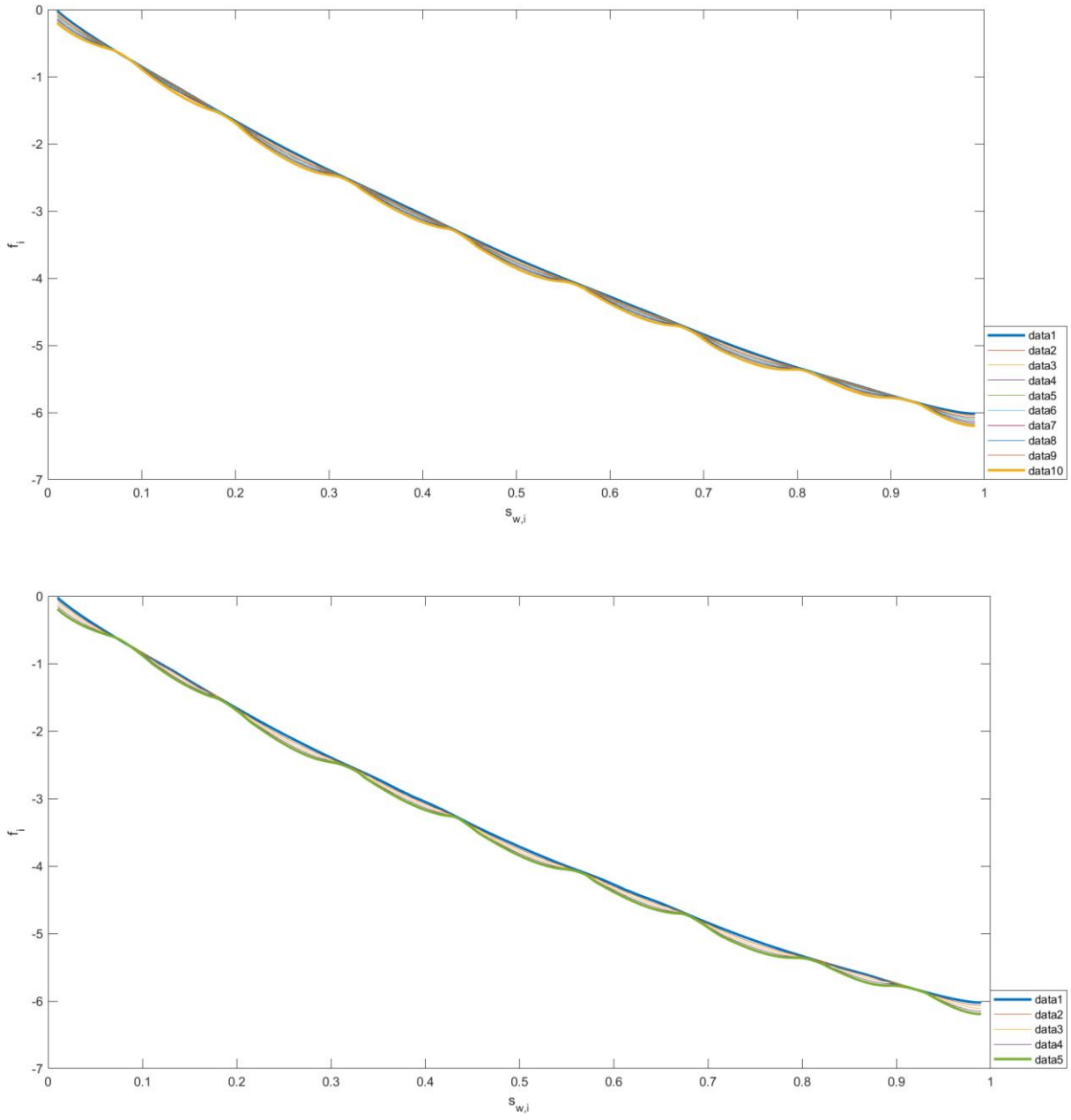


*Figure 5.4. The free energy density vs. compartment saturation diagram for the ten compartments (top) and the five compartments (bottom) in simulations no. 17 and 18, respectively*

The local vs global saturation diagrams show the exact pattern as before, meaning that the upscaling does not impact the local saturations with regards to the global saturations in any specific way including hysteresis in the system.

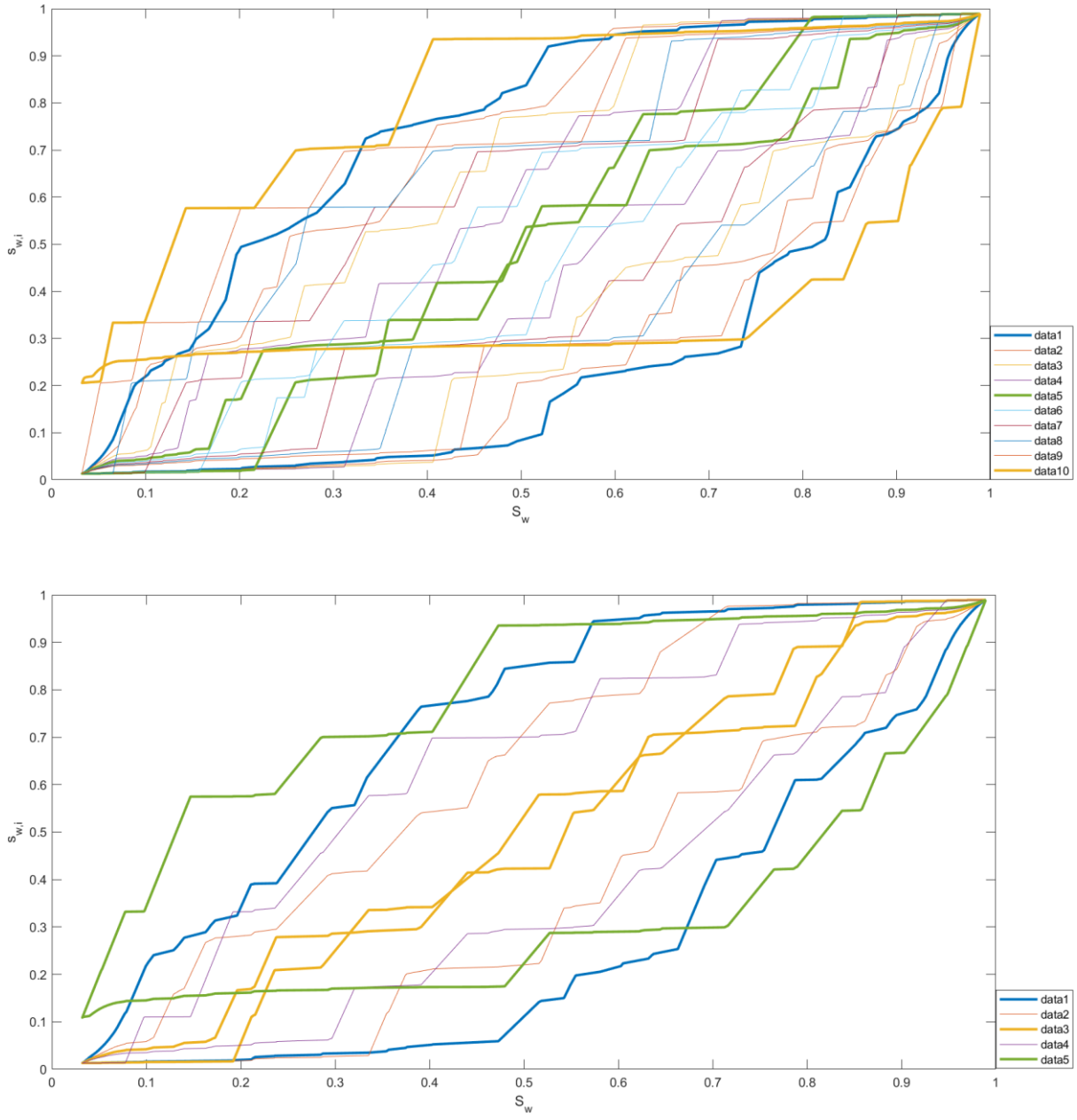


*Figure 5.5. The corresponding compartment- vs. global saturation diagram for the ten compartments (top) and the five compartments (bottom) in simulations no. 17 and 18, respectively*

In the comparison plot of the pressure curves, it can be seen that upscaling does not immensely affect the hysteretic manner caused by the differences in the drainage and imbibition curves rather than the turning saturation at the end of the drainage which indicates a higher residual saturation.

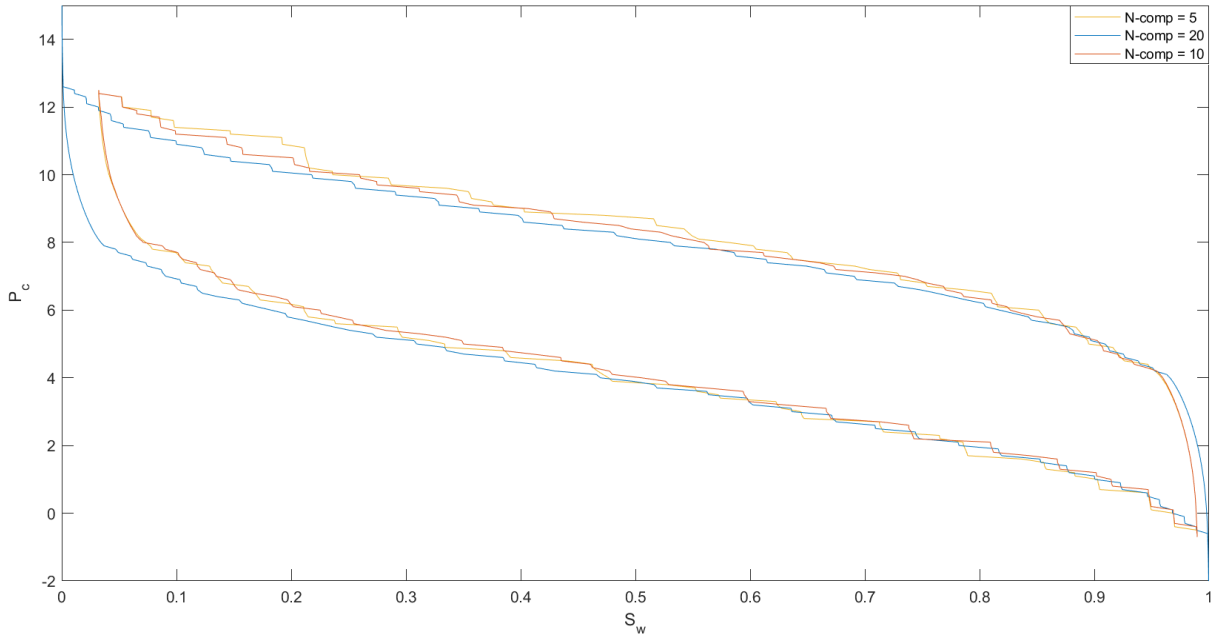


*Figure 5.6. The capillary pressure vs. global saturation curves for simulation no. 16 with twenty compartments (blue), simulation no. 17 with ten compartments (red) and simulation no. 18 with five compartments (yellow)*

# Chapter 6. Conclusion

The discrete-domain model that is presented in this thesis describes the states at which the two-phase flow of the CO2 and water go through during the drainage and imbibition processes at the pore scale, with an emphasis on the irreversibilities of the displacements via the investigation of hysteresis in the capillary pressure and local saturation curves. These so-called irreversibilities stem from the metastable states that are caused by the non-equilibrium essence of the dynamics of multiphase flow in the porous media.

The groundwork of this model relies upon a synthetic energy density function that is obtained based on a series of thermodynamic explanations and relations rather than a sole dependence on the saturation history of the drainage and imbibition processes. The main objective of this study was to investigate the effect of the variations in the input parameters of the model on the hysteretic behaviour of the system in terms of its capillary pressure and local saturations. For this purpose, the model was developed to work under two protocols: Pressure-controlled and saturation-controlled. There are numerous combinations and changes that can be considered for the input parameters in the energy density function, some of which we investigated. According to our results, it can be implied that even the smallest adjustments in the parameters can have noticeable impact on the system exhibiting hysteresis.

For future work, we have recommended for the model to be tested for upscaling from pore scale displacements to larger scales, and an instance of the results have been provided in the previous chapter. Preliminary upscaling simulations show that pressure-saturation curves remain approximately similar under two times of compartment coarsening. Thus, it seems promising to use the discrete-domain model

in a workflow for upscaling capillary pressure curves with hysteresis from pore to core scale. Another suggestion for future work is to construct the energy functions based on data (interfacial areas, pore volume, etc.) from pore scale experiments as a requirement in order to validate the model and to describe realistic cases.

# References


AbdusSatter, Ghulam M.Iqbal. (2016). Reservoir rock properties. In G. M. AbdusSatter, *Reservoir Engineering, The Fundamentals, Simulation, and Management of Conventional and Unconventional Recoveries* (pp. 29-79). Gulf Professional Publishing.

Bertsekas, D. P. (1982 ). *Constrained Optimization and Lagrange Multiplier Methods*. Academic Press.

Blunt, M. J. (2017). *Multiphase Flow in Permeable Media, A Pore-Scale Perspective*. London: Cambridge University Press.

Colin McPhee, Jules Reed, Izaskun Zubizarreta. (2015). Chapter 10 - Relative Permeability. In *Core Analysis: A Best Practice Guide* (pp. 519-653). Elsevier.

E.J. Spiteri, R. Juanes, M.J. Blunt, and F.M. Orr Jr. (2005). Relative Permeability Hysteresis: Trapping Models and Application to Geological CO2 Sequestration. *Society of Petroleum Engineers* , 20.

Enderby, J. A. (1995). The domain model of hysteresis. Part 1 - Independent domains. *Transactions of the Faraday Society*, 835-848.

Gale, J. (2004). Geological storage of CO2: What do we know, where are the gaps and what more needs to be done? *Energy*, 10.

Hassan Hassanzadeh, Mehran Pooladi-Darvish, David W. Keith. (2009). Accelerating CO2 Dissolution in Saline Aquifers for Geological Storage - Mechanistic and Sensitivity Studies. *Energy and Fuels*, 9.

James R. Hunt and Nicholas Sitar. (1988). Nonaqueous Phase Liquid Transport and Cleanup. *WATER RESOURCES RESEARCH*, 12.

Johan Olav Helland, Espen Jettestuen, and Helmer André Friis. (2021). A Discrete-Domain Approach to Three-Phase Hysteresis in Porous Media. *Water Resources Research*, 16.

Johan Olav Helland, Helmer André Friis, Espen Jettestuen, and Svein M. Skjæveland. (2017). Footprints of spontaneous fluid redistribution on capillary pressure in porous rock. *Geophysical Research Letters*, 11.

Kamaljit Singh, Hannah Menke, Matthew Andrew, Qingyang Lin, Christoph Rau, Martin J. Blunt & Branko Bijeljic. (2017). Dynamics of snap-off and pore-filling events during two-phase fluid flow in permeable media. *Nature Scientific Reports*, 13.

Lichao Gao and Thomas J. McCarthy. (2006). Contact Angle Hysteresis Explained. *Langmuir*, 4.

Luis Cueto-Felgueroso and Ruben Juanes. (2016). A discrete-domain description of multiphase flow in porous media: Rugged energy landscapes and the origin of hysteresis. *Geophysical Research Letters*, 8.

M. A. Hesse and A. W. Woods. (2010). Buoyant dispersal of CO2 during geological storage. *GEOPHYSICAL RESEARCH LETTERS*, 5.

Mojgan Hadi Mosleh, Majid Sedighi, Masoud Babaei, Matthew Turner. (2019). Geological sequestration of carbon dioxide. In *Managing Global Warming: An Interface of Technology and Human Issues* (pp. 487-500). Elsevier.

Morrow, N. R. (1970). Physics and Thermodynamics of Capillary Action in Porous Media. *Industrial and Engineering Chemistry* , 25.

Morteza Akbarabadi, Mohammad Piri. (2013). Relative permeability hysteresis and capillary trapping characteristics of. *Advances in Water Resources*, 17.

Mortezaei K, Amirlatifi A, Ghazanfari E and Vahedifard F. (2018). Potential CO2 leakage from geological storage sites: advances and challenges. *Environmental Geotechnics*, 25.

P Zweigel, M Hamborg, R Arts, A Lothe, Ø Sylta, A Tømmerås. (2000). Prediction of migration of CO2 injected into an underground depository: resevoir geology and migration modelling in the sleipner case (North Sea). *Fifth International Conference on Greenhouse Gas Control Technologies* (p. 6). Cairns, Australia: SINTEF Petroleum Research.

R. Juanes, E. J. Spiteri, F. M. Orr Jr., and M. J. Blunt. (2006). Impact of relative permeability hysteresis on. *WATER RESOURCES RESEARCH*, 13.

Reza Ershadniaa, Sassan Hajirezaie, Amin Amooie, Corey D. Wallace,Naum I. Gershenzonc, Seyyed Abolfazl Hosseini, Daniel Murray Sturmer, Robert W. Ritzi, Mohamad Reza Soltanian. (2021). CO2 geological sequestration in multiscale heterogeneous aquifers: Effects of heterogeneity, connectivity, impurity, and hysteresis. *Advances in Water Resources*, 16.

Reza Sedaghatinasab , Shahin Kord , Jamshid Moghadasi , Aboozar Soleymanzadeh . (2021). Relative Permeability Hysteresis and Capillary Trapping during CO2 EOR . *International Journal of Greenhouse Gas Control* , 10.

Sally M. Benson, Ferdinand Hingerl and Lin Zuo, Ronny Pini, Sam Krevor Catriona Reynolds and Ben Niu, Ran Calvo, Auli Niemi. (2015). *Relative permeability for multi-phase flow in CO2 storage reservoirs*. Stanford University .

Samuel Krevor, Martin J. Blunt, Sally M. Benson, Christopher H. Pentland, Catriona Reynolds, Ali Al-Menhali, Ben Niua. (2015). Capillary trapping for geologic carbon dioxide storage – From porescale physics to field scale implications. *International Journal of Greenhouse Gas Control*, 17.

V.T.H. Pham, F. Riis, I.T. Gjeldvik, E.K. Halland, I.M. Tappel, P. Aagaard. (2013). Assessment of CO2 injection into the south Utsira-Skade aquifer, the North Sea, Norway. *Energy*, 12.

Zhonghao Sun and J. Carlos Santamarina. (2019). Haines jumps: Pore scale mechanisms. *Physical Review E*, 7.